UKAEA-CCFE-PR(22)23

K. Verhaegh, B. Lipschultz, J.R. Harrison, N. Osborne, A. Williams, P Ryan, J. Allcock, J. Clark, F. Federici, B. Kool, T. Wijkamp, A. Fil, D. Moulton, O. Myatra, A. Thornton, T.O.S.J. Bosman, C. Bowman, B. Duval, S. Henderson, R. Scannell, the MAST Upgrade team, the EuroFusion MST1 team

Spectroscopic investigations of detachment on the MAST Upgrade Super-X divertor

Spectroscopic investigations of detachment on the MAST Upgrade Super-X divertor

K. Verhaegh, B. Lipschultz, J.R. Harrison, N. Osborne, A. Williams, P Ryan, J. Allcock, J. Clark, F. Federici, B. Kool, T. Wijkamp, A. Fil, D. Moulton, O. Myatra, A. Thornton, T.O.S.J. Bosman, C. Bowman, B. Duval, S. Henderson, R. Scannell, the MAST Upgrade team, the EuroFusion MST1 team

This is a preprint of a paper submitted for publication in
Nuclear Fusion

Spectroscopic investigations of detachment on the MAST Upgrade Super-X divertor

K. Verhaegh[1], B. Lipschultz[2], J.R. Harrison[1], N. Osborne[3], A. Williams[1,2], P. Ryan[1], J. Allcock[1], J.G. Clark[1,3], F. Federici[2], B. Kool[4,5], T. Wijkamp[5,4], A. Fil[1], D. Moulton[1], O. Myatra[1,2], A. Thornton[1], T.O.S.J. Bosman[4,5], C. Bowman[2,1], G. Cunningham[1], B. Duval[6], S. Henderson[1], R. Scannell[1] the MAST Upgrade team* and the EuroFusion MST1 team*∗

[1] Culham Centre for Fusion Energy, Culham, United Kingdom
[2] York Plasma Institute, University of York, United Kingdom
[3] University of Liverpool, Liverpool, United Kingdom
[4] Dutch Institute for Fundamental Energy Research DIFFER, Eindhoven, The Netherlands
[5] Eindhoven University of Technology, Eindhoven, The Netherlands
[6] Swiss Plasma Centre, École Polytechnique Féérale de Lausanne, Lausanne, Switzerland
* See author list of "J. Harrison et al 2019 Nucl. Fusion 59 112011 (https://doi.org/10.1088/1741-4326/ab121c)
*∗ See author list of "B. Labit et al 2019 Nucl. Fusion 59 086020 (https://doi.org/10.1088/1741-4326/ab2211)

E-mail: `kevin.verhaegh@ukaea.uk`

Abstract.

In this paper we present the first analysis of the atomic and molecular processes at play during detachment in the MAST-U Super-X divertor using divertor spectroscopy data. Our analysis indicates the existence detachment in the MAST-U Super-X divertor can be separated into four sequential phases: First, the ionisation region detaches from the target at the detachment onset leaving a region of increased molecular densities downstream of it. The plasma interacts with these molecules, resulting in molecular ions (D_2^+ and/or $D_2^- \rightarrow D + D^-$) which further react with the plasma, leading to excited atoms and significant Balmer line emission; Molecular Activated Recombination and Dissociation (MAR and MAD). Secondly, the MAR region detaches from the target with a sub-eV temperature region downstream of it. Thirdly, the onset of strong emission from electron-ion recombination (EIR) occurs. Fourthly, the electron density decays near the target, resulting in the movement of a density front upstream from the target.

The analysis in this paper indicates that plasma-molecule interactions play a critical role in the amount and interpretation of hydrogen atomic line emission characteristics on MAST-U, having a larger impact on the hydrogen Balmer line series than previously found. Furthermore we find that the Fulcher band emission profile in the divertor can be used as a proxy for the ionisation region and can, as well, be employed as a plasma temperature diagnostic for improving the separation of hydrogen emission arising from electron-impact excitation and that from plasma-molecule interactions.

We provide evidences for the presence of low electron temperatures (< 0.5 eV) during detachment phases III-IV. That analysis is based on quantitative spectroscopy analysis, a Boltzmann relation of the high-n Balmer line transitions as well as an analysis of the brightness of high-n Balmer lines.

Keywords: Tokamak divertor; Molecules; plasma; SOLPS-ITER; Plasma spectroscopy; Detachment; MAST Upgrade

1. Introduction

Power exhaust is a major challenge for the realisation of fusion energy as the expected un-mitigated target heat fluxes in a reactor can be significantly higher than the tolerable engineering limits at the target [1, 2]. The heat load reductions that can be obtained by by increased radiation alone are limited ‡ as they result in an increased ion target flux. The heat flux arising from surface recombination of those ions can exceed target engineering limits in reactor conditions if the upstream parallel energy flux density is sufficiently high. The target ion flux can be reduced through divertor detachment, during which plasma-atom/molecule interactions result in simultaneous power, particle and momentum removal in the divertor. Detachment is obtained when the target electron temperatures reaches relatively low values ($T_t <\sim 5$ eV), which can be achieved by neutral recycling (e.g. higher upstream densities / fuelling) and/or extrinsic impurity seeding (increased radiative dissipation).

Alternative Divertor Configurations (ADCs) aim to utilise variations in the divertor magnetic topology to enhance power exhaust in three different ways. First, they are designed to facilitate larger power reductions of the parallel heat flow into the divertor before reaching the target, than currently achieved in 'conventional' divertors. Secondly, they are designed to increase the operational space of detachment (e.g. 'detachment window' [4, 5]) by reducing the detachment onset thresholds (e.g. lower density or lower impurity fraction needed to access detachment). Thirdly, magnetic topology variations can enhance the 'controllability' of detachment, by reducing the sensitivity of the displacement of the front-edge of the cold, detached, plasma (e.g. detachment 'front') to a 'physics' control parameter (e.g. density, upstream heat flux, impurity fraction). This 'detachment sensitivity' is defined as s $\partial L_{pol}/\partial C$ where L_{pol} is the distance between the target and the front of the detached plasma and the target in poloidal (parallel) space and C is a set of 'physics' control parameter(s) [4, 6, 5, 7, 8] §. Both an increase of the detachment window as well as larger power dissipation in the divertor would allow, if successful, the operation of future tokamak reactors with lower core impurity fractions and radiation, which would benefit core and fusion performance. Depending on the precise reactor parameters required, using ADCs may be essential [9].

---

‡ They are limited to a factor 4-5 (not considering magnetic shaping) [3]

§ Theoretical investigations in the reduced detachment sensitivity of ADCs have so far only been performed under steady-state conditions

The Mega Amp Spherical Tokamak - Upgrade (MAST-U) is a new spherical tokamak [10, 11, 12], based at the Culham Centre for Fusion Energy (CCFE) in the United Kingdom. MAST-U has been built specifically for investigating ADCs to 1) determine their enhanced divertor performance and feasibility; and 2) use magnetic shaping to improve our understanding of plasma-edge physics. MAST-U includes a tightly baffled divertor chamber [11], which facilitates a baffled double-null Super-X Divertor (SXD) [6].

The SXD employs an increase in the target radius compared to the Conventional Divertor (CD) leading to significant 'total flux expansion', which is predicted by analytic and SOLPS-ITER models to reduce the detachment onset threshold [4, 5, 6], increase the detachment window and reduce $\partial L_{pol}/\partial C$ [4]. Despite the theoretical benefits of the Super-X divertor, analysis of TCV tokamak experimental results initially did not support such predictions [7] due to the openness of the, then non-baffled [7], TCV divertor [13].

Apart from the increased target radius and resultant total flux expansion, it is also important to trap the neutrals in the divertor region [13]. On MAST-U, this is achieved using tight baffling at the entrance to the divertor, which increases both neutral trapping/compression [6]. Keeping neutral trapping constant while the divertor configuration is varied is required to test the benefit of increased total flux expansion [13]. The above predictions of the positive effect of total flux expansion are in agreement with preliminary results from MAST-U, which have strong reductions in the target heat and particle flux in Super-X Divertor (SXD), compared to the Conventional Divertor (CD).

MAST-U started operations in late 2020 and has finished its first physics campaign. In general, as expected from predictions discussed above, operation using the Super-X divertor resulted in the divertor plasma being detached, except for extremely low upstream densities. Thus it is critical to study the underlying physics processes to ascertain whether existing models include the proper physics. This work provides the first investigation of the plasma-atom and molecule interaction processes at play throughout the entire detached operational space of the MAST-U Super-X divertor. We have found that the level of detachment can be separated into four different phases. Those phases start with the detachment of the ionisation region from the target and end with the detachment of the entire recombination region from the target, the latter suggesting the decay of electron density near the target and upstream movement of the electron density front off the target surface.

The basis for the above statements on detachment phases is based on analysis of data from line-of-sight spectroscopy through the Super-X divertor chamber. The 'intensity' (e.g. brightness in $ph/m^2/s$) of various hydrogen Balmer line intensities as well as part of the D_2 Fulcher band (595 to 615 nm), has been monitored during detachment. Using the BaSPMI analysis developed previously [14, 15, 3, 16], the Balmer line brightnesses have been been decomposed into their respective atomic and molecular emission components and are discussed below for each phase of detachment. Detailed analysis of the $n = 9-20$ Balmer lines is performed to provide evidence for low density ($n_e < 10^{19} m^{-3}$) and temperature conditions ($T_e \ll 0.5$ eV).

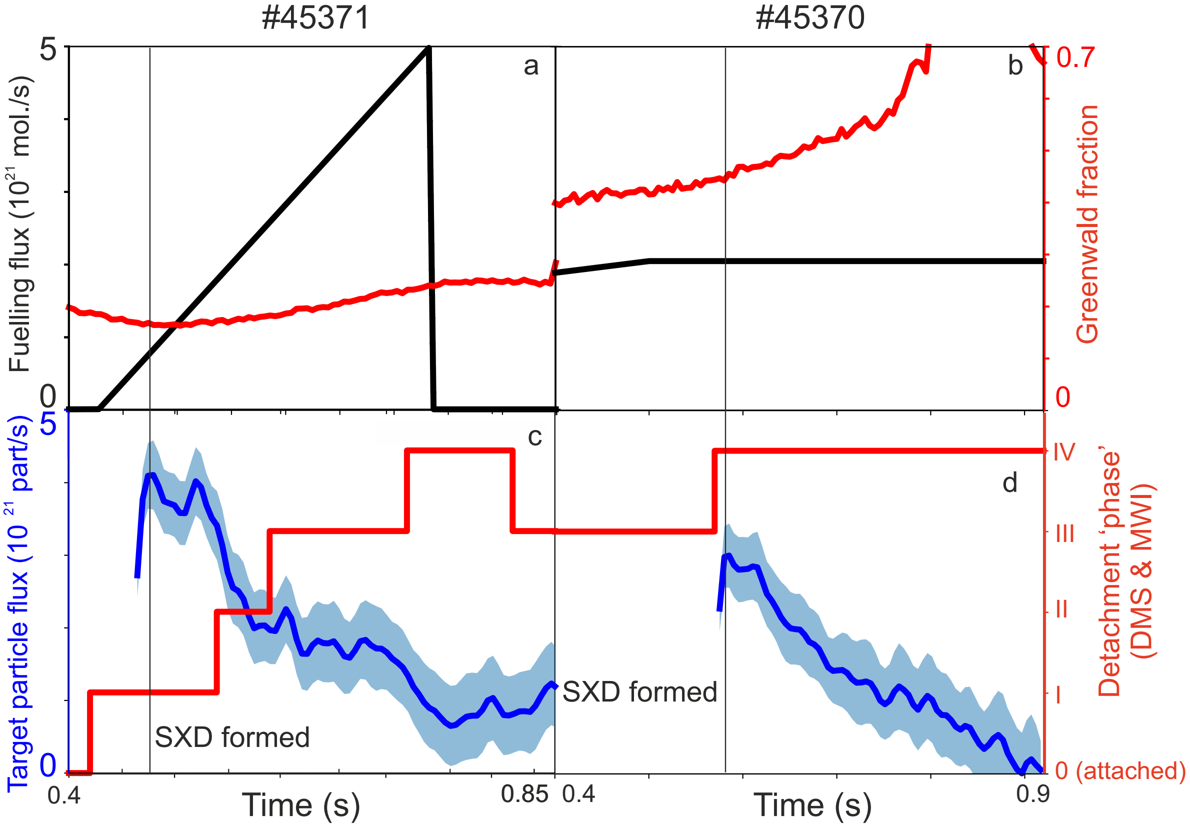

Figure 1. Overview of discharges # 45370 and # 45371. a,b) Core electron density and fuelling traces. c, d) Total lower outer target integrated particle flux over 'tile 5' (figure 2), together with indicated divertor detachment phase based on spectroscopy (see section 3).

Our analysis shows plasma-molecule interactions have a major role in the interpretation of hydrogen Balmer line measurements on MAST-U; consideration of such effects is critical for the interpretation of any MAST-U hydrogen spectroscopy or imaging data.

2. MAST Upgrade overview

Figure 1 shows fuelling and core density data, as well as the evolution of the total target particle flux, as function of time for pulse # 45371 (plasma current, $I_p = 650$ kA), the main discharge used in this work, and pulse # 45370, which is operated at a lower plasma current ($I_p = 450$ kA) and is more deeply detached; The level of detachment is delineated by the detachment phase given, based on spectroscopic analysis (see section 3). After the divertor is formed, # 45371 employs fuelling from the lower divertor valve ('LFS-D-b', shown in figure 2 a) whereas # 45370 employs the default midplane fuelling on the MAST-U inner wall ('HFS' - see figure 2 b)). The values obtained for the lower outer target integrated particle flux should be interpreted qualitatively at this stage, as there are some gaps in the Langmuir probe coverage at the outer target.

To perform the studies described in this paper, a new line-of-sight Divertor Monitoring Spectroscopy (DMS) system has been developed and commissioned. These lines of sight originate from two different lens-fibre set-ups - V1 and V2 (figure 2 b). The DMS uses two spectrometers ('DMS-York' in purple; 'DMS-CCFE' in green) with interleaved lines of sight to monitor two spectral regions simultaneously. For discharge # 45371, the two spectrometers are used to monitor: 1) the $n = 5, 6$ Balmer lines using a medium resolution (0.1 nm) setting and 2) part of the D_2 Fulcher band (595 - 615 nm) and $D\alpha$ (656 nm) simultaneously using a low resolution setting (0.4 nm). The latter employs a shortpass filter to attenuate the $D\alpha$ brightness so it is more similar to that of the D_2 Fulcher band. For discharge # 45370, DMS-York monitored the high-n ($n \geq 9$) Balmer lines simultaneously (365 - 385 nm) using a high resolution (0.06 nm) setting, whereas DMS-CCFE monitored the CIII (465 nm) and $D\beta$ Balmer line (486 nm) (not used in this work).

In addition to the line-of-sight DMS spectroscopy system, a Multi-Wavelength Imaging (MWI) is used to obtain images of spectrally filtered emission from the divertor [17, 18]. The MWI has 10 different channels such that 10 different spectral filters can be used to monitor 10 different spectral lines/bands simultaneously: this includes the D_2 Fulcher band as well as the $n = 3, 4, 5, 6, 7, 9$ Balmer lines. Although the MWI data has not been used in the analysis employed in this paper, its observations are qualitatively consistent with the DMS observations and are occasionally referred to throughout the paper.

3. Spectroscopic MAST-U Super-X detachment observations and their interpretation

Our analysis of the DMS data (which is consistent with the MWI) indicates that detachment in the MAST-U Super-X divertor can be separated in four different phases, which are shown schematically in figure 3.

(i) Detachment onset: the ionisation front detaches from the target and moves towards the divertor entrance, leaving behind a region where plasma-molecule interactions involving molecular ions result in excited atoms leading to a majority of the Balmer line emission. These molecular ions include D_2^+ created from molecular charge exchange (non-dissociative ionisation $e^- + D_2 \rightarrow D_2^+ + 2e^-$ occurs at higher temperatures in the ionisation region) and possibly $D_2^- \rightarrow D^- + D$. The same interactions also result in significant amounts of Molecular Activated Recombination (MAR) and Dissociation (MAD) and thus contribute as an energy sink, particle (ion) sink and neutral atom source [3]. Although a quantitative power/particle balance analysis is outside of the scope of this paper, the clear separation of Balmer line emission associated with electron-impact excitation and plasma-molecule interactions (figure 4 A I) suggests that MAR & MAD associated power/particle losses are dominant over atomic ones below the ionisation region in this phase.

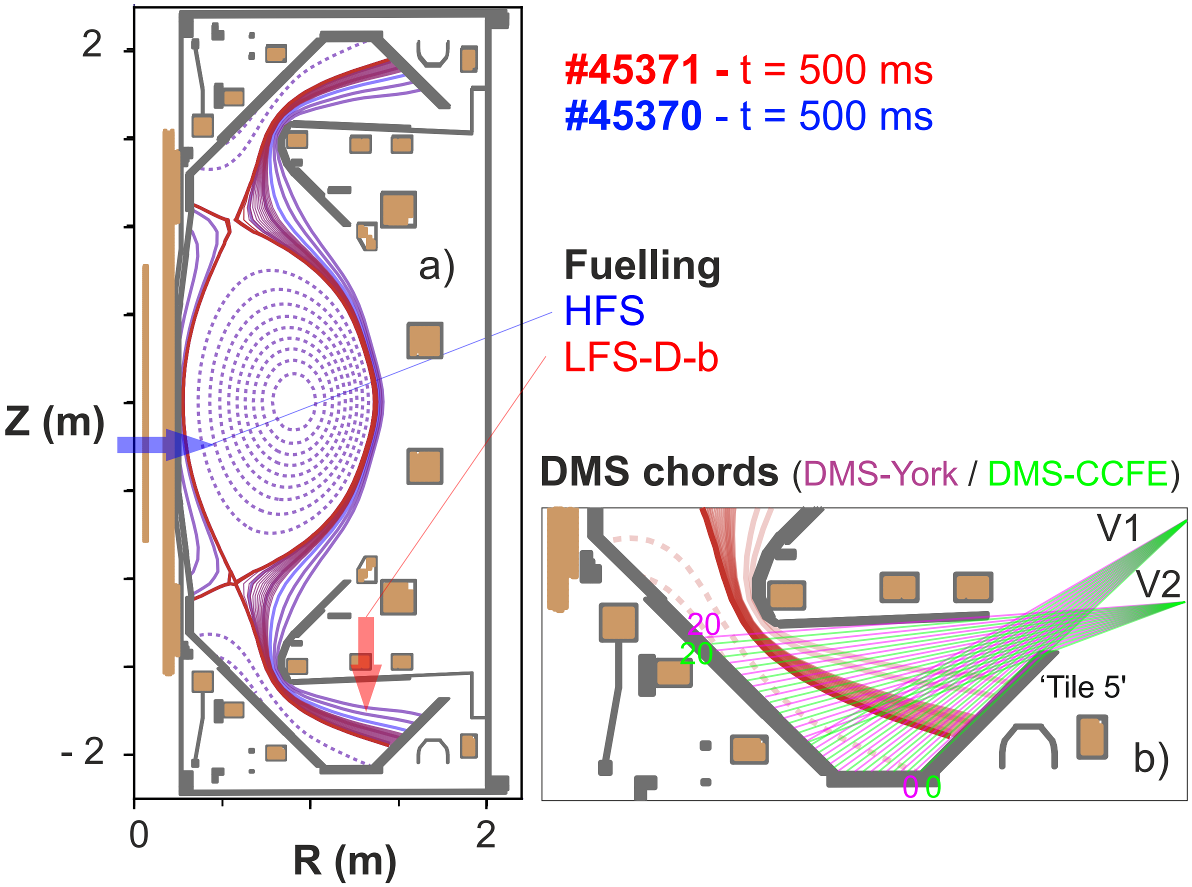

Figure 2. a) The magnetic geometries corresponding to the two discharges # 45371 and # 45370 at 500 ms, are shown together with the vessel geometry, poloidal field magnets and the fuelling valve locations utilized ('HFS' and 'LFS-D-b'). b) Just the lower divertor region is shown along with the DMS spectroscopic chordal lines-of-sight originating from view points V1 and V2, which are both coupled to two spectrometers ('DMS-York' and 'DMS-CCFE'). In both a) and b), the Super-X separatrix strike point is incident on 'Tile 5'

(ii) The probability of converting molecules into molecular ions is greatly reduced at low plasma temperatures ($T < 1$ eV) as (see section Appendix A and [3]): 1) vibrational excitation of the molecules promotes the creation of molecular ions and collisions between the plasma and the molecules plays a role in this; 2) some ion energy (e.g. temperature) is needed in order to promote molecular charge exchange ($D^+ + D_2 \rightarrow D_2^+ + D$). As a result, the peak in Balmer line emission associated with molecular ions detaches from the target as the target electron temperature drops to values ($T_e < 1$ eV) where the rate at which D_2 is converted into molecular ions is reduced. This also implies a movement of the MAR and MAD regions from the target [3].

(iii) Appearance of strong electron-ion recombination (EIR) emission near the target. At this point, EIR could start to dominate over MAR as an ion sink: quantitative power/particle balance is subject of future work.

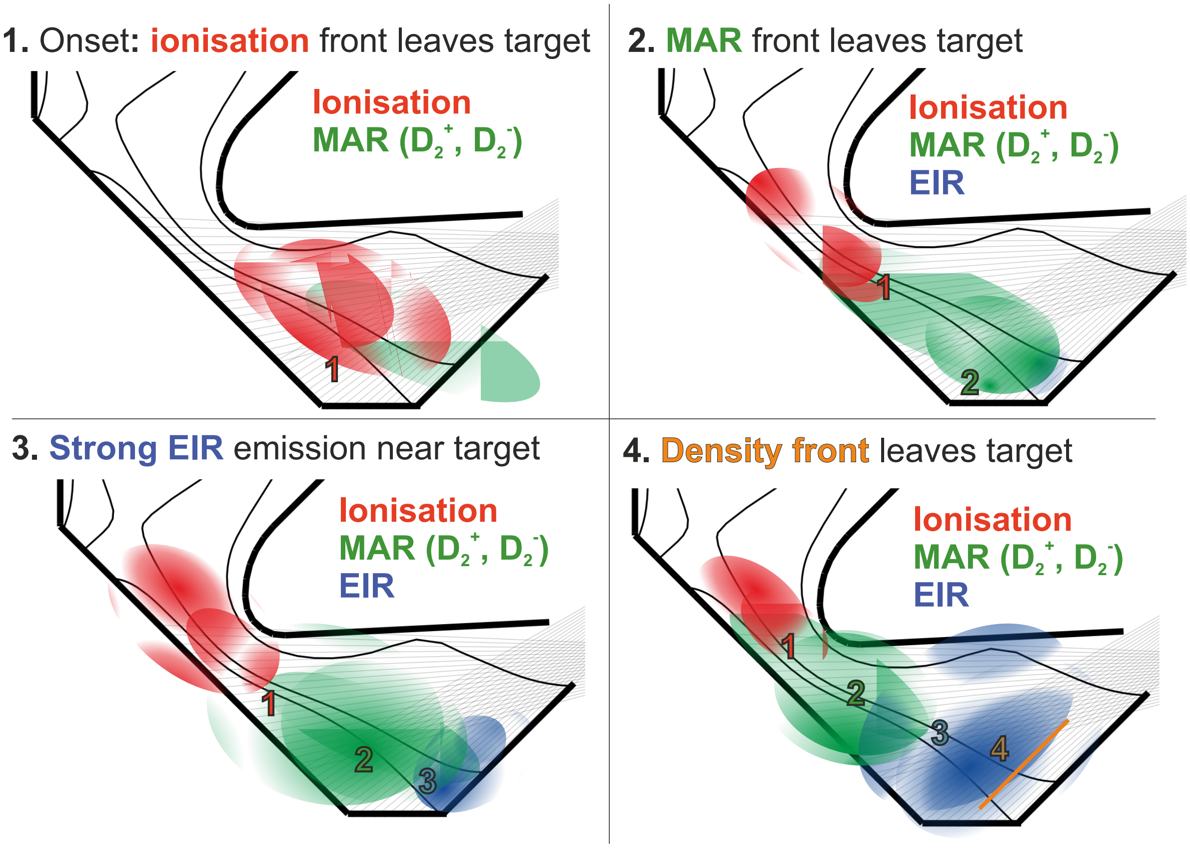

Figure 3. Schematic overview of the four inferred MAST-U Super-X detachment phases. Also shown is the Super-X plasma geometry and the DMS spectroscopic viewing chords. The numbers shown indicate: (1) the back-end of the ionisation region; (2) the back-end of the Molecular Activated Recombination (MAR) region; (3) the front-end of the Electron Ion Recombination (EIR) region; and (4) the back-end of the electron ion recombination / density region.

(iv) The electron-ion recombination-related emission region detaches from the target and moves towards the divertor entrance; this suggests that the electron density peak moves away from the target.

Figure 4 shows observations of the hydrogen emission profiles and Balmer line ratios during the four identified different phases for discharge # 45371. These phases are, however, general in the (unseeded) MAST-U Super-X divertor and have been observed at various plasma currents, variations in super-X geometries (e.g. relatively low poloidal flux expansion, relatively high poloidal flux expansion, different strike point locations on tile 5 (figure 2) of MAST-U) and fuelling locations (upper divertor, lower divertor, high field side, low field side).

In addition, figures 4 A I -IV also shows the results of a quantitative analysis of the Balmer line emission data using the BaSPMI methodology [15, 16] to separate the hydrogen Balmer line emission into its various atomic and molecular interaction contributions, which can be ultimately used to estimate contributions to ion sources/sinks (ionisation / electron-ion recombination / molecular activated recombination (MAR) /

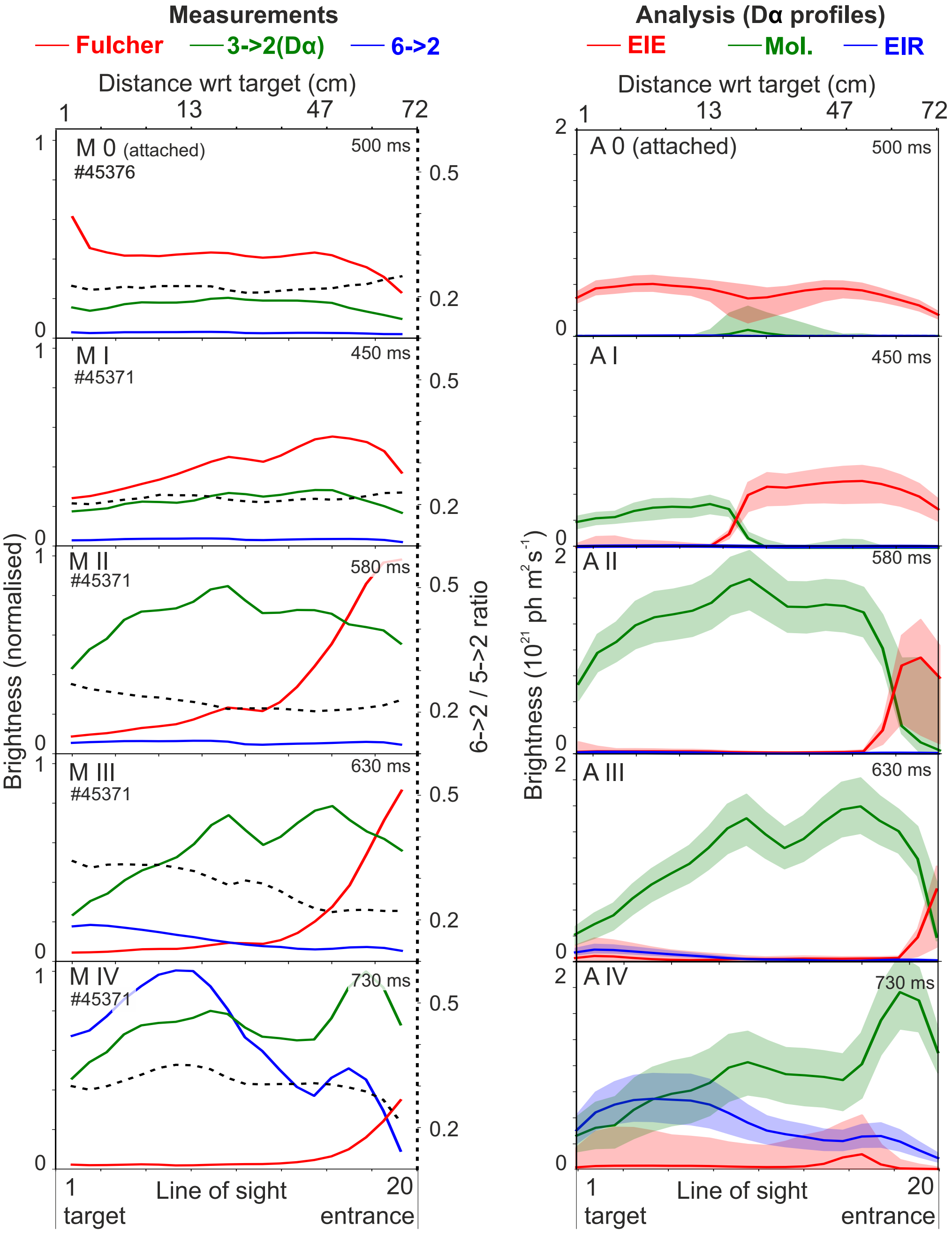

Figure 4. (M 0) through (M IV): Measured and normalized brightness profiles in the lower divertor during MAST-U pulse # 45371 (M I - M IV) and # 45376 (M 0 - attached) for the Fulcher band (595-615 nm), $n = 3, 6$ Balmer lines as well as the $6 \to 2/5 \to 2$ Balmer line ratio along the various spectroscopic chords at four different times, spanning the attached regime (0) and the four phases of detachment (I-IV). A 0) through A IV): Analysed BaSPMI [16, 14] from measurements M 0 - M IV showing the brightness profiles of the $D\alpha$ associated with electron-impact excitation ("EIE" of D), plasma-molecule interactions ("Mol." of D_2, D_2^+, D^-) and electron-ion recombination ("EIR" of D^+). The indicative poloidal distance, along the divertor leg, between the target and intersection of the line-of-sight with the separatrix are shown on top. The 'EIE', 'Mol.' and 'EIR' emission regions are indicative of the 'ionisation', 'MAR & MAD' and 'EIR' regions, respectively [3].

molecular activated ionisation (MAI)) and radiative power losses from excited atoms. The way BaSPMI is applied is further discussed in Appendix C. The BaSPMI analysis has been independently compared against a new Bayesian analysis approach (Appendix C.1).

3.1. Detachment phase 1: ionisation movement and MAR appearance

Before the detachment onset, we generally observe a roughly flat profile of the $n = 3, 5, 6$ Balmer lines as well as the Fulcher band emission (with some slight peaking near the target) along the various spectroscopic lines of sight, together with Balmer line ratios suggestive of electron-impact excitation. This can be observed in figure 4 M 0 and A 0, which have been obtained from # 45376 at 500 ms, which is the same scenario as # 45371 but employs fuelling in the upper divertor instead of lower divertor, as # 45371 is never fully attached.

These observations are similar to those previously found on TCV [19, 20, 3], where a strong correlation between the Fulcher band emission and the ionisation region were found [3, 15]. Given the differences of the neutral atom and molecule mean free paths, it was argued for TCV [15] that the Fulcher emission throughout the entire divertor leg is evidence of molecules entering the divertor leg radially. This is also suspected to be true for the MAST-U case shown.

At the start of # 45371, which starts near the detachment onset, the Fulcher emission region detaches from the target (figure 4 M I). As the plasma fuelling is further increased, the downstream-end of the Fulcher emission region moves from near the target towards the divertor entrance. Whilst this is occurring, the Balmer line ratios remain constant over the entire divertor leg and the Balmer line emission remains roughly constant over the entire divertor, as shown in figure 4 M I.

The combined observations of the Fulcher emission region, Balmer line ratio and Balmer line intensity are key to demonstrating how Balmer line intensities can lead to misleading results if the possibility of molecular break-up resulting in excited atoms is not considered. Without considering these molecular effects, the ionisation region would be expected to be near the target. This would be inconsistent with the Fulcher emission observation, which suggests that the region near the target is too cold to electron-impact dissociate molecules (and thus too cold for ionising atoms).

In section 4.2, the importance of the Fulcher emission brightness is further discussed and it is shown that the Fulcher emission profile could be employed as a temperature diagnostic. A lack of Fulcher band emission in a region with a significant molecular density is associated with electron temperatures that are too low for significant electron-impact excitation of hydrogen to occur. Therefore, the movement of the *downstream-end of the Fulcher emission* region, combined with the flat Balmer line emission profile and line ratio, is suggestive of a movement of the *ionisation* region, consistent with previous research [3]. Conversely, the *lack-of Fulcher emission* near the target (where there should be a high molecular density), combined with the flat Balmer line emission profile and line ratio, is suggestive of the onset of plasma-molecule interactions involving D_2^+ and possibly D^- resulting in molecular activated recombination (MAR).

This qualitative description is in agreement with a quantitative analysis using BaSPMI [15], which is used to decompose the $D\alpha$ emission profile into its various atomic and plasma-molecule related processes, shown in figure 4 A I. In this BaSPMI application, the peak normalised downstream-end of the Fulcher emission profile (along the various chords) has been used to provide a constraint for the analysis of the electron temperature, which is described in Appendix C.

As fuelling is increased, the electron-impact excitation emission region is observed to move quickly from near the target to almost near the divertor entrance. This is shown more clearly in figure 5, which shows the contributions to the $D\alpha$ brightness profile, inferred by BaSPMI, as function of poloidal distance from the target, which has been calculated based on the intersection between the DMS chords and the separatrix [‖]. The electron-impact excitation emission region is correlated with the ionisation region and the observed evolution of the emission region implies a movement of the ionisation region.

3.2. Detachment phase 2: movement of MAR region and obtaining sub-eV temperatures

As the fuelling is further increased, the Fulcher emission moves further towards the divertor entrance and ultimately a region of MAR related emission starts to move from the target towards the divertor entrance, figure 4 II and A II. Plasma-molecule interactions leading to MAR involving D_2^+ and/or D^- below 5 eV require the presence of $D_2(\nu)$ molecules that are excited to relatively high vibrational levels [21, 3]. Most of this vibrational excitation likely arises from plasma-molecule collisions. Below a certain temperature, however, both the level of highly vibrationally excited molecules drops (as the plasma has insufficient energy to promote vibrational excitation) and the ions have insufficient energy to promote molecular charge exchange. This results in a significantly reduced D_2^+/D_2 ratio [3, 22] with decreasing T_e that is stronger than the increase of the molecular density with decreasing T_e. More detailed analysis, shown in section 4.1, indicates that this temperature is roughly associated with ~ 0.8 eV. One caveat, however, is that the actual temperature corresponding to the peak of the MAR emission moving is strongly sensitive to the distribution of vibrational states, for which a simplified model is used in the AMJUEL rates [22] employed in section 4.1. Therefore, this 0.8 eV point should not be interpreted as a fixed point, but rather evidence for the appearance of sub-eV temperatures. More detailed work analysing the distribution of vibrational levels through Fulcher band spectroscopy is currently ongoing to test such models. The movement of the MAR emission region is consistent with the BaSPMI analysis presented in figure 4 A II.

As the fuelling increases further, the back-end of the MAR region moves further and further from the target until it reaches the divertor entrance. This would suggest

---

[‖] Note that the measurement capability is limited to 0.8m due to the chords not poloidally sampling beyond the entrance to the outer divertor.

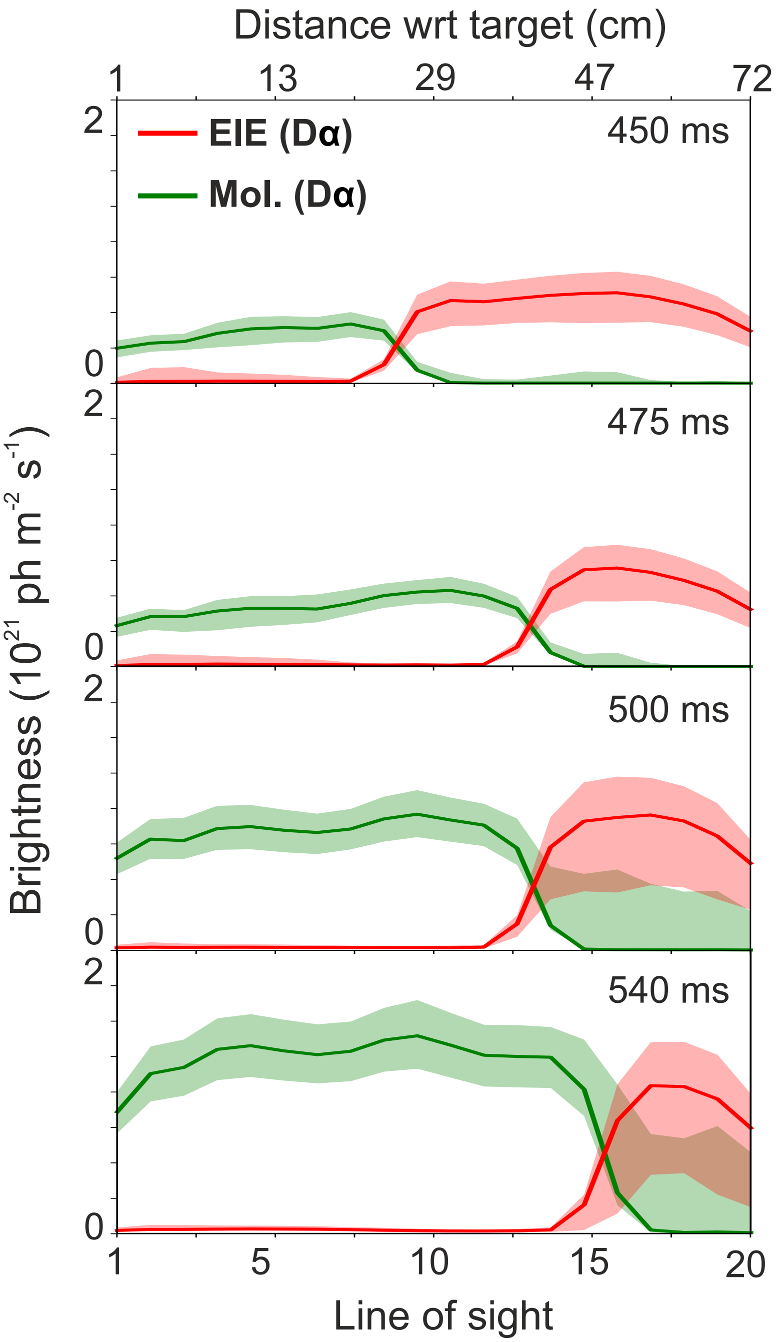

Figure 5. BaSPMI analysis results of the different $D\alpha$ emission contributions (electron-impact excitation ('EIE' - red) and plasma-molecule interaction related emission ('Mol.' - green)) at a few time points during the first detachment phase (between 450 and 580 ms) as function of line of sight. The indicative poloidal distance, along the divertor leg, between the target and intersection of the line-of-sight with the separatrix are shown on top. Electron-ion recombination has been omitted as it is negligible in phase I. The 'EIE' and 'Mol.' emission regions are thus indicative of the 'ionisation' and 'MAR' regions, respectively [3].

that the majority of the divertor chamber has achieved sub-eV electron temperatures.

The movement of regions described is consistent with the in-depth BaSPMI analysis, which indicate that indeed the $D\alpha$ emission associated with plasma-molecule interactions ('Mol.') starts to decay near the target. This suggests a movement of the MAR region upstream from the target.

3.3. Detachment phase 3: appearance of strong signs of electron-recombination

As fuelling is further increased, the Fulcher emission region moves out of the spectroscopy view, into the divertor throat, the MAR emission region moves towards the divertor throat and ultimately a strong increase in both $n = 6$ Balmer line intensity as well as the $n = 6/5$ Balmer line ratios observed near the target, shown in figure 4 III. This is suggestive of strong emission contributions from electron-ion recombination below the MAR emission region, which particularly contribute to high-n Balmer lines. Our BaSPMI analysis of figure 4 A III indicates that the EIR contribution for the $n = 5, 6$ Balmer line is 80-90% and 90-95 % near the target, respectively, although this is smaller for $D\alpha$ (figure 4 A III). This analysis suggests that the increase in the $n = 5, 6$ Balmer line brightness is expected to be correlated to the appearance of the high-n ($n \geq 9$) Balmer line spectrum.

Such a high-n Balmer line spectrum has been measured for discharge # 45370. Quantitative analysis of the high-n Balmer line spectra has been performed by fitting the entire high-n Balmer line spectra ($n = 9 - 20$) at once using both a Stark broadening model [16, 23] as well as a Boltzmann distribution for the ratio between the intensity of the various high-n Balmer lines [24, 25]. An example of a fit result obtained from # 45370 is shown in figure 6. This result is representative and similar analysis results have been obtained for a range of different discharges, including a range of different plasma currents.

The obtained fit results suggest the presence of a low electron density ($n_e \ll 1 \times 10^{19} m^{-3}$) and temperature ($\ll 0.5 eV$ - ($0.1 - 0.2$ eV based on a Boltzmann fit [24, 25])) region. These temperatures and densities can be considered as EIR emission weighted quantitaties along the line of sight [20, 14] - as such they may not correspond to the separatrix temperature. Those low electron density estimates are qualitatively consistent with the Inglis-Teller limit [26]: after averaging over 15 frames ($\sim 200 ms$) up to $n = 21$ Balmer line observed beyond which there is insufficient signal to detect individual Balmer lines; which suggests $n_e < 1.6 \times 10^{19} m^{-3}$.

Such low electron densities ($n_e < 2 \times 10^{19} m^{-3}$ (attached, detachment onset and phase II detachment) - dropping to $n_e \ll 10^{19} m^{-3}$ in phase III & IV) and electron temperatures ($T_e \ll 1$ eV from phase II onwards) are qualitatively consistent with results obtained from the MAST-U divertor Thomson scattering (DTS) system [27]: for # 45371 DTS measurements indicate $n_e \sim 10^{19} m^{-3}$ during detachment phases I-II and $T_e < 0.5$ eV (below the detection limit) during detachment phases III-IV.

A consistency check for the estimated electron temperatures can be obtained from

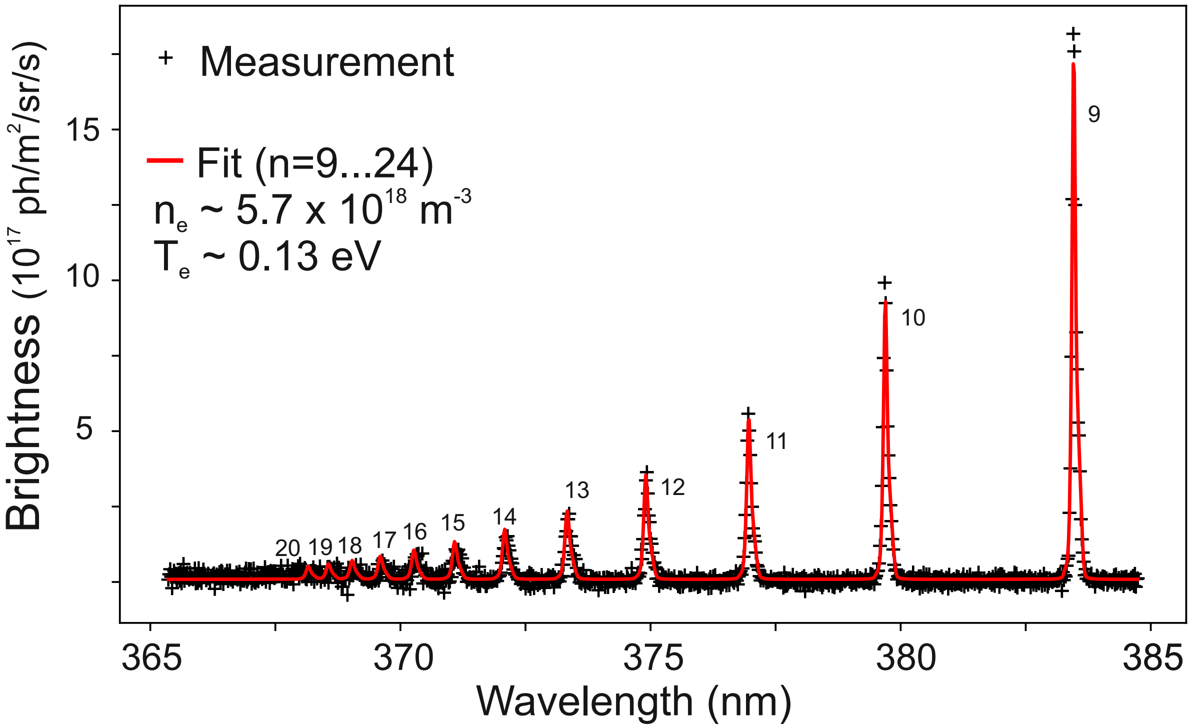

Figure 6. Measured high-n Balmer line spectra for line of sight # 10 (midway divertor) at 670 ms for # 45370, together with a high-n Balmer line fit (red). n_e and T_e (using a Boltzmann distribution) are inferred from the high-n Balmer line fit, indicating a low electron density/temperature regime. The $n = 9$ brightness in this case is $4 \times 10^{18} phm^{-2}s^{-1}$.

the monitored high-n Balmer line emission brightness: for a given electron density (n_e), the monitored brightness depends on the length of the emission region along the line of sight (ΔL) as well as the electron temperature (T_e): $B_{n\geq 9\rightarrow 2} \approx \Delta L n_e^2 PEC^{rec}_{n\geq 9\rightarrow 2}(n_e, T_e)$, where $PEC^{rec}_{n\geq 9\rightarrow 2}(n_e, T_e)$ is the recombination emission coefficients for high-n Balmer lines which depends on n_e and increases exponentially with decreasing T_e. For a known n_e, T_e, a required emission length can thus be estimated ($\Delta L \approx \frac{B_{n\geq 9\rightarrow 2}}{n_e^2 PEC^{rec}_{n\geq 9\rightarrow 2}(n_e,T_e)}$), which decreases for decreasing T_e as $PEC^{rec}_{n\geq 9\rightarrow 2}$ increases. If we assume $T_e = 0.2$ eV (ADAS default temperature limit [28]), one would require a pathlength of 1.6 m near the target and 0.2 m near the divertor entrance at $t = 600$ ms. As ΔL can only be a maximum of 20-40 cm physically (based on multi-wavelength imaging measurements of the $n = 9$ Balmer line from the Multi-Wavelength Imaging (MWI) diagnostic [17]), this provides further evidence for the $T_e = 0.1 - 0.2$ eV regime obtained from the Boltzmann fit.

This consistency check assumed that the emission of high-n Balmer lines (e.g. $n \geq 9$) is only due to electron-ion recombination. This has been verified by post-processing the BaSPMI analysis output from # 45371 to estimate the contribution of plasma-molecule interactions to high-n ($n \geq 9$) Balmer lines. The result for the $n = 9$ Balmer line is shown in figure 7. This indicates that the high-n ($n \geq 9$) Balmer line emission may, at most, have a 10 % contribution of plasma-molecule interactions during the onset of detachment

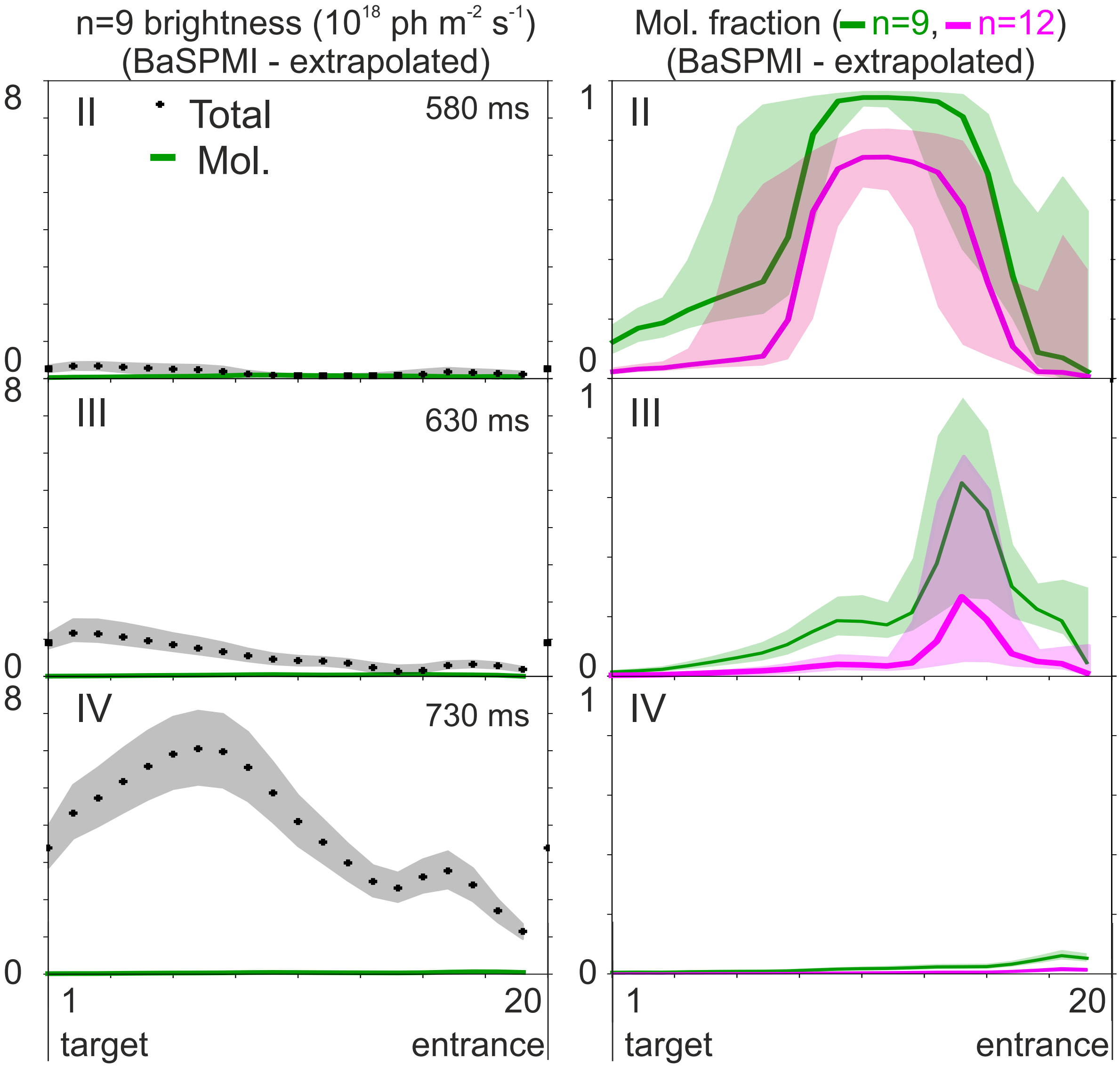

Figure 7. Extrapolated total and plasma-mol. related contribution ('Mol') to the $n = 9$ Balmer line emission for # 45371 during phases II, III, and IV, together with the fraction of the $n = 9$ (green) and $n = 12$ (magenta) Balmer line emission due to plasma-molecule interactions.

phase III. Although the contribution of plasma-molecule interactions to the $n = 9$ Balmer line is larger before EIR starts to occur, the contribution of the $n = 9$ Balmer line emission is at most $10^{17} phm^{-2}s^{-1}$, which would result in $4 \cdot 10^{16} phm^{-2}s^{-1}sr^{-1}nm^{-1}$. As is clear from figure 6, this would be below the detection threshold (despite the data in figure 6 being averaged over 3 frames to an effective acquisition frequency of 25 Hz to improve the S/N level).

Inferences of electron temperatures below 0.2 eV during phases III and IV of detachment are supported by the in-depth BaSPMI analysis for # 45371. BaSPMI estimates the recombination rate by relating the intensity of the EIR part of the medium-n Balmer line brightness [16], $B^{rec}_{n\rightarrow 2}$, to a recombination rate. Along that curve, the electron temperature varies and the maximum reference model value for $B^{rec}_{n\to 2}$ is obtained at the ADAS limit of 0.2 eV. BaSPMI analysis for # 435371 indicates that during detachment phases III-IV (figure 4 A III and A IV) the spread of inferred values for $B^{rec}_{6\to 2}$ exceeds the spread of maximum reference values for $B^{rec}_{n\to 2}$. This suggests the recombination temperature is below 0.2 eV where the emission coefficients for EIR are higher, increasing the maximum reference value.

3.4. Detachment phase 4: density front emission movement

With increased fuelling the EIR region further expands, Fulcher emission becomes almost invisible in the divertor chamber and the MAR peak reaches the divertor entrance. Ultimately, the back-end of the EIR emission region leaves the target (figure 4 IV). At this point all monitored Balmer line emission detaches from the target. As mentioned in the previous section, the dominant Balmer line emission process at this point is electron-ion recombination (figure 4 A III, AIV). Considering that the temperature profile in the divertor must decrease or stay constant when going along the divertor leg towards the target, a drop in the electron-ion recombinative emission must imply an electron density drop near the target. As fuelling is increased, the back-end of the EIR emission region moves further and further towards the divertor entrance, indicating a significant movement of the electron density front. This is qualitatively supported by estimates of the electron density for # 45371 (using only the $n = 6$ Balmer line) which drops from $\sim 2.4 \times 10^{19} m^{-3}$ to $\sim 1.6 \times 10^{19} m^{-3}$. Although this difference was found to be robust when performing Monte Carlo uncertainty propagation, these numbers should not be used as a quantitative measure since the Stark width is much smaller than the instrumental width at these densities. This is likely also the reason why these estimates are higher than the measurements obtained through divertor Thomson scattering, which are more in line with the electron estimates obtained through fitting the high-n Balmer line spectra using a Stark broadening model (figure 8): $n_e \sim 10^{19} m^{-3}$ before the density decrease near the target.

100 ms before the ramp-down of # 45371 (figure 1 a), we employ a fuelling cut and observe how the divertor responds. This causes the peak in MAR emission to move back into the divertor chamber, the downstream-end of the EIR emission region to move back towards the target and the electron densities to rise again near the target (not shown) within 50 ms.

There are other discharges in which detachment is deeper, such as # 45370, which ultimately ends in a disruption brought on by a MARFE. As this discharge has high-n Balmer line coverage, the electron density front movement has been analysed in more detail by fitting the entire high-n Balmer line spectra using a Stark broadening model (see figure 6). The obtained $n = 9$ brightnesses together with the inferred electron densities are shown in figure 8. Here the EIR emission region moves closer towards the divertor entrance as time progresses (higher fuelling levels). The movement of the EIR region is correlated with a sharp decay of the inferred electron density near the target,

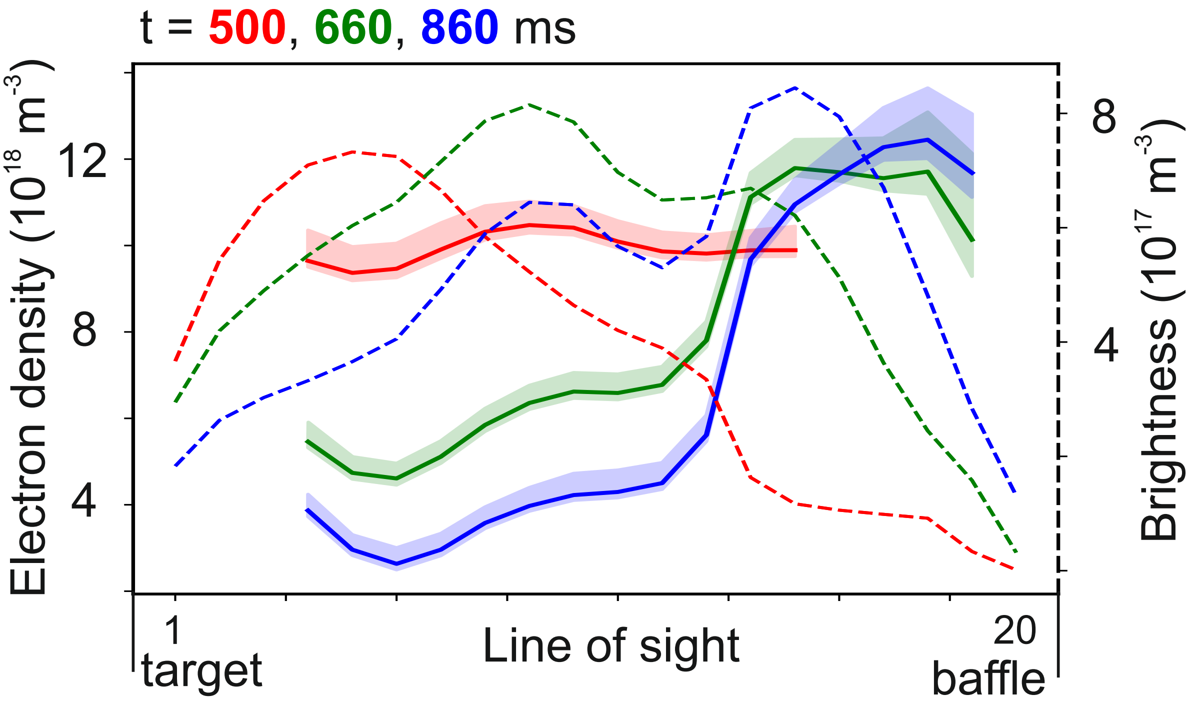

Figure 8. Spatial profiles, from near the target to the divertor baffle, of $n \geq 9$ (summed) Balmer line brightness (dotted lines) as well as inferred electron densities from Stark broadening (solid lines) at 500 (red), 670 (green) and 860 (blue) ms of # 45370.

resulting in an electron density front that moves from the target towards the x-point, providing quantitative evidence for the electron density front movement.

4. Discussion

4.1. Understanding the impact of plasma-molecule interactions on hydrogen emission on MAST-U

In section 3.1 it was shown that the Fulcher emission region had detached from the target whilst there was still significant Balmer line emission near the target corresponding to line-ratios consistent with (but not actually from) Electron-Impact Excitation (EIE) (as opposed to Electron-Ion Recombination (EIR)), which illustrated that Plasma-Molecule Interactions (PMI) can greatly impact the Balmer line spectra. This is investigated in more detail by performing simplified emission modelling (Appendix A) to investigate Balmer line emission trends at $n_e = 10^{19} m^{-3}$ using MAST-U molecular density scalings from SOLPS-ITER simulations [29] and at $n_e = 7 \cdot 10^{19} m^{-3}$ using TCV molecular density scalings from SOLPS-ITER simulations [30] in figure 9, which shows that:

- Emission from excited atoms after molecular break-up (PMI), which is dominated by emission from excited atoms after the break-down of D_2^+, results in very similar line ratios to EIE - figure 9 a,b; which is significantly lower than line ratios from

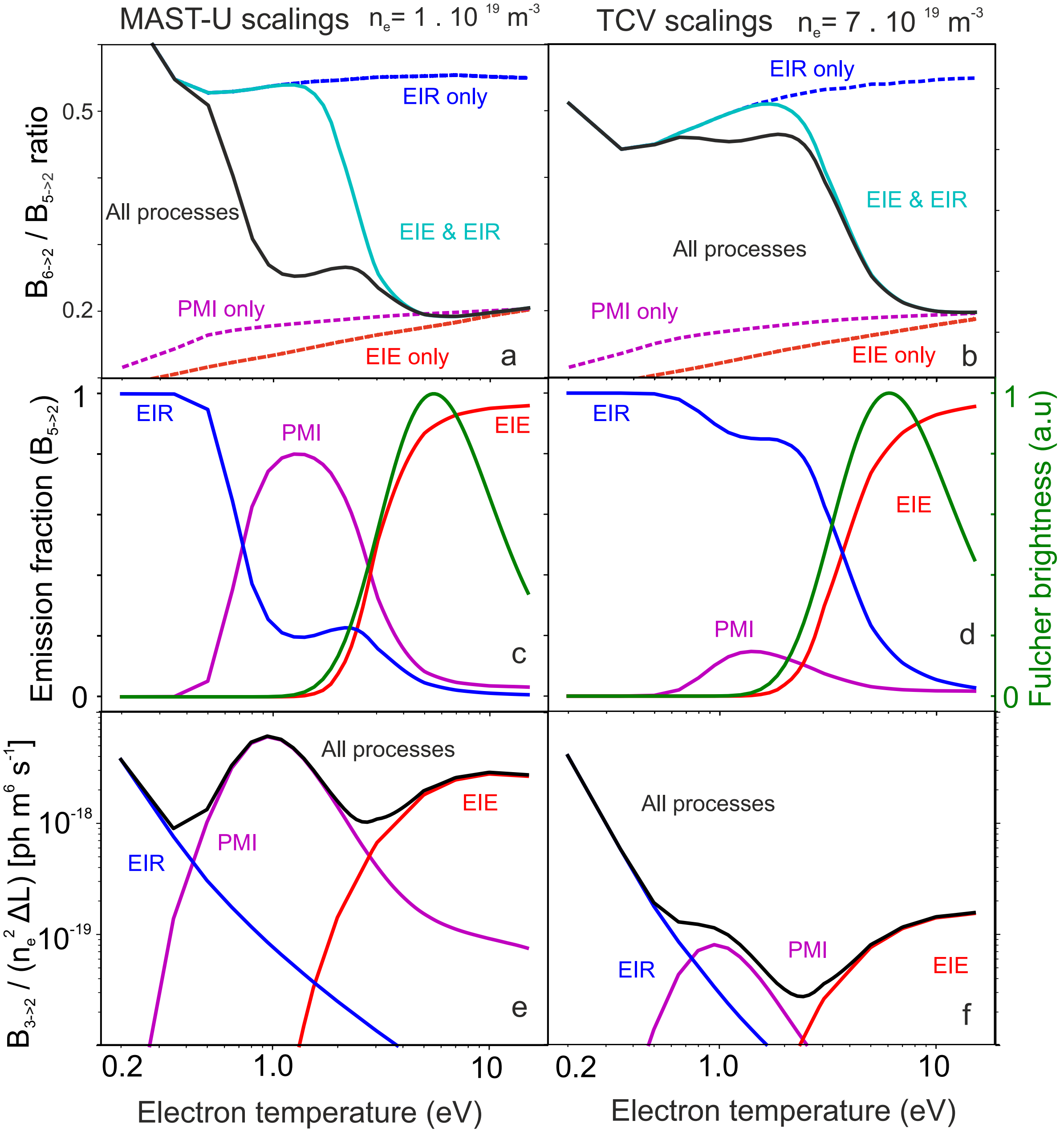

Figure 9. Simplified Balmer emission modelling at two different electron densities using MAST-U and TCV molecular density scalings, respectively. Note that these scalings for TCV have been derived in an open divertor geometry (before the installation of baffles). a, b) The $n = 6/n = 5$ Balmer line ratio is shown as function of T_e when only atomic effects are included (cyan) and when all processes are included (black). Blue, red, magenta dotted lines show the expected EIR, PMI and EIE only trends. c, d) The $n = 5$ Balmer line emission fractions are shown as function of T_e for EIR, PMI and EIE as well as the normalised expected Fulcher emission brightness. e, f) The $D\alpha$ ($n = 3$) brightnesses, divided by $\Delta L n_e^2$, of EIR, PMI and EIE as well as the total are shown as function of T_e.

an Electron Ion Recombination (EIR) emission dominant plasma. Therefore, PMI reduces the Balmer line ratio if both EIR and PMI are present. As a result, the line ratio transitions from a low value (EIE & PMI) to a high value (EIR) at lower temperatures when PMI is included (black curve) compared to cases without PMI (cyan curve), when the the MAST-U densities and scalings are used (figure 9 a). Therefore, analysing Balmer line emission measurements in MAST-U conditions without considering PMI could lead to gross misinterpretations (up to orders of magnitude) of the ionisation source for $T_e = [0.4 - 7]$ eV. Comparing figures 9 a and b shows that PMI lowers the maximum obtained Balmer line ratio for the TCV scalings, rather than moving the T_e at which the Balmer line ratio transitions from a high value to a low value. Therefore, the impact of ignoring PMI would be smaller on the ionisation source estimates for TCV-like conditions (although it can still be significant [15]).

- The Fulcher emission brightness is well correlated with the electron-impact excitation emission, which re-inforces that the Fulcher band can be used as a rough indicator for the ionisation region, which is further discussed in section 4.2. Additionally, comparing figures 9 a and c shows that the MAST-U observed separation (in T_e space) between the Fulcher emission region and the Balmer line ratio increase is expected when molecular effects are considered.
- At temperatures below 1 eV, the PMI related emission is reduced as the likelihood of creating D_2^+ from D_2 through molecular charge exchange (e.g. $D_2(\nu) + D^+ \rightarrow D_2^+ + D$) is reduced. This results in the formation of a PMI $D\alpha$ emission region (figure 9 e), which shows that several $D\alpha$ emission regions or 'fronts' are expected to be formed, corresponding with EIE (and thus ionisation), PMI (and thus MAR) and EIR (figure 9 e). The precise T_e to which the peak in PMI corresponds is sensitive to the used model for the vibrational distribution (e.g. towards lower T_e / higher T_e for an underestimation / overestimation of the highly vibrationally excited D_2 population). This explains why the four different detachment phases can be identified based on monitoring the $D\alpha$ emission on MAST-U and why the $D\alpha$ emission detaches from the target (e.g. $T_e <\sim 1$ eV).

Comparing the Balmer line ratio trends at lower and higher densities explains some, but not all, of the differences between the MAST-U observations and the TCV observations in [19, 20, 15, 3, 31]. EIR scales $\propto n_e^{2-3}$ and exponentially with decreasing T_e. The electron density difference between the MAST-U and TCV model cases alone results in a $\sim \times 60$ difference in the EIR magnitude. Therefore, EIR will become significant at lower temperatures for lower electron densities. Due to the electron density difference, there is a larger region below the Fulcher emission region where the line ratio is consistent with EIE & PMI, complicating the separation of these two effects more on MAST-U than on TCV (figure 9 a,b). An important caveat of this analysis is that these simulations for TCV have an un-baffled divertor. The TCV divertor currently, however, can be baffled [32]. This could bring the scalings more in line with those of MAST-U, which is something that needs further investigation.

Apart from the higher electron densities on TCV, there are two other effects which could explain the difference between these MAST-U and previous TCV observations. First, the PMI inferences on TCV have remained peaked near the target as the electron temperatures in the TCV divertor, at the time, did not drop below 1 eV. Secondly, the D_2/D ratio (molecular density to atomic density) is roughly 2.5 times higher on MAST-U than on TCV according to the scalings obtained from SOLPS-ITER simulations, discussed in Appendix A. As a result, PMI dominates over EIE at higher temperatures on MAST-U than compared to TCV. This, combined with higher electron densities in TCV, results in a significantly smaller contribution of PMI to the Balmer line emission on TCV (figure 9 d), although the general trends remain similar.

Conclusively, considering PMI is important for the TCV conditions to get out MAR estimates and to get a higher accuracy on the ionisation source during deep detached conditions [15, 14, 3]. In contrary, on MAST-U considering PMI is essential even for basic ionisation estimates from Balmer line spectroscopy.

4.2. Usage of the Fulcher emission region to identify movements in the ionisation front

In section 4.1 we have shown that there is a correlation between the temperatures where the Fulcher band emits and where electron-impact excitation and atomic ionisation occurs. This shows promise for using the Fulcher band brightness as a diagnostic for the temperature regime as well as using it as an identifier for the detachment front, which are more quantitatively investigated below.

First, we investigate the suitability of using the Fulcher brightness trend as a temperature diagnostic. This is obtained by modelling the Fulcher band brightness as function of T_e, while accounting for the $\Delta L n_{D_2}$ trend used in section 4.1 and derived in Appendix A. Monte Carlo uncertainty propagation is used to include a large uncertainty in the derived $\Delta L n_{D_2}$ trend. The calculation details for this are shown in Appendix B. The Fulcher band brightness as function of T_e leads to a peaked profile and the trailing (low T_e) edge of the profile is correlated to a temperature window, as shown in figure 10. These curves indicate that the trailing edge of the Fulcher emission region can be used as a temperature constraint in the 1.3 - 4.5 eV range. Below / above this range, it can provide a maximum / minimum temperature constraint, respectively. The calculation details for this are shown in Appendix B.

Apart from using the trailing edge of the Fulcher emission profile as a method to constrain the electron temperature, the narrow uncertainties obtained in figure 10 - plus the fact that the curves from MAST-U and TCV are similar - suggest that by tracking the trailing edge 'front' it may be possible to track an electron temperature region of the plasma, which could also be used as a proxy for the 'detachment front'. Future work is planned to track the Fulcher emission front and compare its evolution against analytic models that predict the evolution of the detachment front [4].

Secondly, we investigate the suitability of using the Fulcher emission brightness as a

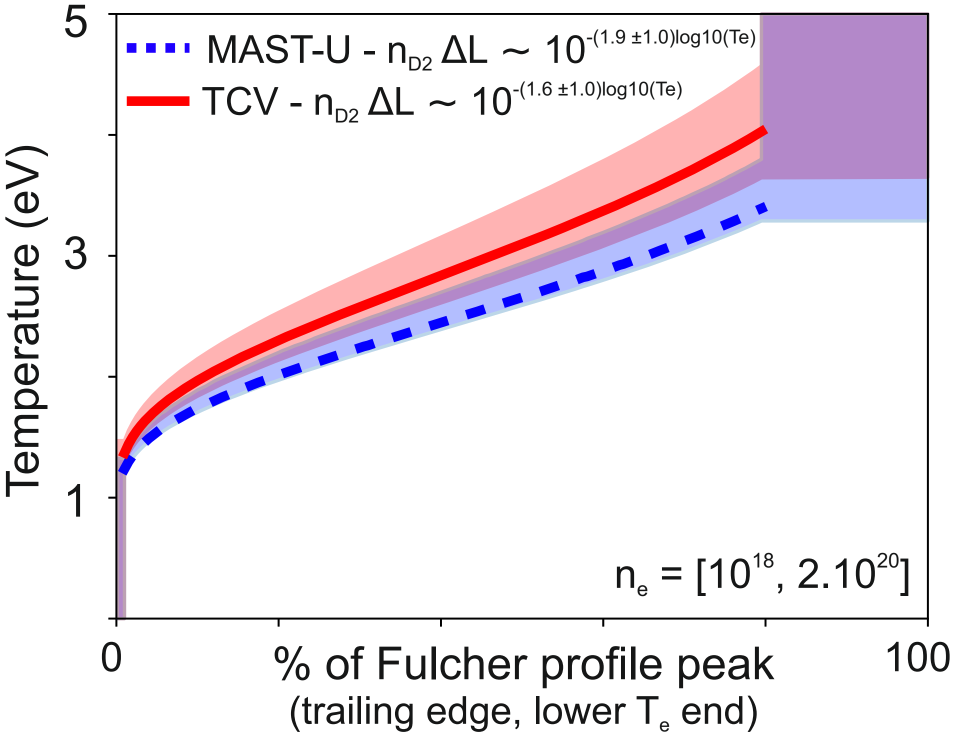

Figure 10. Monte Carlo uncertainty propagation analysis linking the trailing edge of the Fulcher emission profile (between 1 and 80 % of its peak intensity) to a possible temperature range (68 % confidence). Below/above this range, it can provide a maximum / minimum temperature constraint, respectively.

diagnostic for the ionisation region by employing a synthetic diagnostic to SOLPS-ITER simulations to monitor the line-integrated Fulcher emission brightness ($\propto ph/m^2/s$) as well as the line-integrated atomic ionisation source ($ion/m^2/s$) employing synthetic divertor spectrometers DSS for TCV [19] and the DMS for MAST-U (figure 2). Those two trends are plotted as function of each other in figure 11, which indicates a strong correlation between the Fulcher emission brightness and the ionisation region, particularly at decaying levels of the ionisation source (which corresponds to lower temperatures ($T_e \ll 5$ eV)). Such a correlation is found for MAST-U (density scan and seeded cases) as well as TCV (density scan). The correlation during a density scan for TCV and MAST-U are almost identical (on a log-log plot), despite the different plasma conditions, different molecular / neutral densities and different chordal integrals. During N_2 seeding, however, the obtained correlation is different.

One caveat, however, is that the mean free path for atoms and molecules is different. Although they both become larger than the divertor leg during detached regimes, in attached conditions (for the studied regimes) the neutral atom mean free path is on a similar order to the divertor size while that of molecules is up to 5 cm. Therefore, in higher electron temperature conditions the correlation between the Fulcher emission region and the ionisation region is expected to worsen (which is also observed in figure 11).

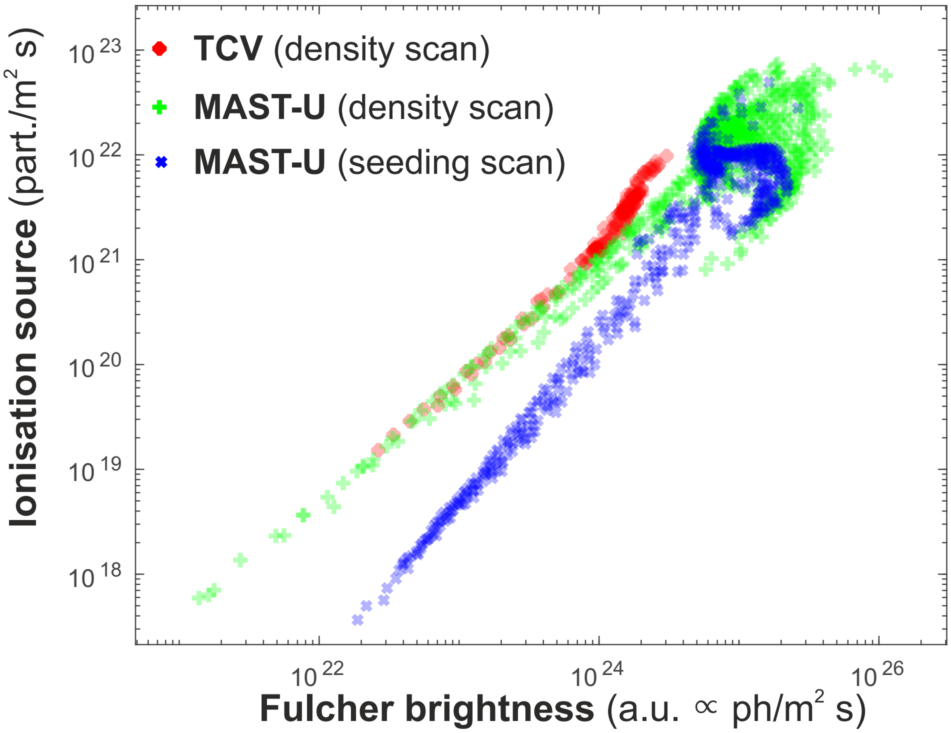

Figure 11. The chordal-integrated (atomic) ionisation source plotted as function of the chordal-integrated Fulcher emissivity (a.u.) using synthetic diagnostics applied to SOLPS-ITER simulations (5 simulations TCV, density scan [30]; 15 simulations MAST-U (density scan) [29] and 19 simulations MAST-U (N_2 seeding scan) [29]. The experimental spectroscopy chord descriptions of TCV (32 lines of sight, pre-baffles [19]) and MAST-U (40 lines of sight, figure 2, no interleaving) have been used to determine the result.

For smaller mean free paths, such as in reactor-relevant conditions, the molecules would be dissociated before reaching the point where the resulting atoms are ionised. As a result, the Fulcher emission would be expected to be more localised and around the ionising region. Therefore, indeed, both could be spatially separated by a distance in the order of the mean free path of a neutral atom. However, given that the mean free paths are small in a reactor, the Fulcher emission region and ionisation regions should still be close together.

If the Fulcher emission region could be used as a proxy for the ionisation region, this may give rise to using real-time control techniques in conjunction with filtered camera imaging [33, 34, 18] to control the ionisation region in real-time, which would be a major step forward towards detachment control.

4.3. Implications, relevance and accuracy of our findings

Our preliminary analysis on MAST-U suggests the presence of a wide operational regime for detachment in the Super-X configuration, exhibiting four distinct phases of detachment. As shown during # 45370, the core density can be increased further, even in the ultimate phase of detachment, leading to a significant density front movement of ~ 50 cm from the target before the plasma disrupts due to a MARFE. Additionally, in # 45371 it was shown that a gas cut during the ultimate detachment phase (e.g. phase IV - density front movement) could move the density front downstream towards the target. These results suggest that detachment is relatively 'stable' on MAST-U. This may have been facilitated by the predicted reduction of the detachment sensitivity (in steady-state) to a 'physics' control parameter [4], such as upstream electron density, in the Super-X divertor. Further studies on the detachment sensitivity are required, for instance by identifying the various detachment fronts using spectrally filtered imaging and comparing these against model predictions.

One challenge with this, however, is the large operational window of detachment and the lack of a single sensor diagnostic to monitor the entire detachment domain. For example, one could track the evolution of the ionisation region to investigate detachment sensitivity. However, as shown, once the detachment reaches its second phase, the ionisation goes out of the view of the DMS diagnostic (as well as for other diagnostics which operate within the divertor chamber, such as the MWI). Therefore, it is likely that different sensors are needed in different detachment regimes. For instance, one could track the ionisation front in phase I detachment, the MAR emission front in phase II-III detachment and the EIR emission back-end in phase IV of detachment. This also has implications for real-time detachment control strategies. It may be possible that future sensitivity studies using the imaging bolometry could be used over a larger portion of the detachment window, as it has an x-point view. These results also suggest that it would be beneficial to add other diagnostics with x-point views, such as a second multi-wavelength imaging system.

In this work, modest divertor densities have been found ($n_e < 2{\times}10^{19} m^{-3}$), combined with strikingly cold divertor conditions ($T_e \ll 0.5$ eV), for which various forms of evidence have been presented. Despite the plasma current of 650 kA (which is higher than the 340 kA TCV plasma current of previous studies [3, 20]), these electron densities are significantly smaller than on TCV or according to existing, non-interpretive, SOLPS-ITER modelling for MAST-U [29, 5]. The reason for this is likely the low detachment threshold (Greenwald fraction < 0.2) as the divertor electron density stops increasing in fairly deep detachment phases, which are achieved relatively early during a density ramp in the MAST-U Super-X divertor. One key difference between the previous simulations and these experimental results is that the presented results are from Ohmic L-mode plasmas, whereas beam power is used in the simulations. Higher power discharges are thus likely required to fully test the MAST-U Super-X divertor, as is evidenced by the fact that in a large part of the detachment window, the ionisation in the divertor chamber is negligible. Although this raises questions on the relevance of these regimes for reactors, the fact that such deeply detached conditions can be obtained while keeping the core plasma relatively stable is promising for detachment stability and control.

Our results indicate that plasma-molecule interactions, particularly interactions that involve vibrational excitation of the molecular cloud resulting in the formation of molecular ions (D_2^+ & $D_2^- \rightarrow D + D^-$) that react with the plasma, are particularly strong for MAST-U: the clear transition between electron-impact excitation and emission from plasma-molecule interactions suggests a clear transition between an ionising plasma and a plasma dominated by MAR and MAD (figure 5). One concern is that such interactions are not fully included in SOLPS-ITER simulations: interactions with molecular ions in a deuterium plasma are essentially negligible if the default SOLPS-ITER reaction set-up is used [3]. Even if such interactions are included through modified reaction rates, the vibrational distribution of the molecules is not modelled in SOLPS-ITER and instead a simplified model is employed to model the vibrational distribution based on the local plasma parameters (n_e, T_e) [22, 35]. Such a model may be incorrect as interactions between the molecules and the walls, as well as transport of vibrationally excited molecules can be important [36]. Given the importance of plasma-molecule interactions in the MAST-U divertor, it is therefore particularly important to investigate the transport and wall effects of (vibrationally) excited molecules in the MAST-U divertor.

An important element to the relevance of our findings for reactors is that reactors based on alternative divertor configurations likely employ a strategy that involves a more deeply detached divertor, compared to reactor strategies based on a conventional divertor divertor design. Given the strong trade-off between the ionising region and the region that involves plasma-molecule interactions with molecular ions, plasma-molecule interactions could play an important role in the configurations where the ionisation region is kept significantly detached from the target. This would likely involve reactors that employ alternative divertor configurations.

The achievement of the low temperature regimes have implications for requirements on atomic/molecular data development. By default, ADAS data is available until 0.2 eV [28, 37]. This results in additional uncertainty in the atomic/molecular physics coefficients used in our BaSPMI analysis, which effectively uses nearest neighbour extrapolation (section Appendix C). The appearance of low electron temperatures also has implications for plasma-edge codes such as SOLPS-ITER, which employs ADAS data as well as AMJUEL data. The AMJUEL data validity limits likely need further investigating when simulations are performed that operate in deeply detached MAST-U Super-X conditions.

An important caveat to the presented analysis is that we assume that the plasma is optically thin. This could not be verified experimentally as there was no divertor VUV spectroscopy available during the first MAST-U campaign. If the plasma is not optically thin, it could greatly impact the analysis results, as explained in [14, 15], as it could have a strong impact on the reaction rates as well as the emission coefficients [38, 39]. Although photon opacity may occur in MAST-U conditions [3, 40], this is expected to occur at much higher powers and electron densities (by more than an order of magnitude) [40]. However, this would need further investigation in future MAST-U campaigns.

The presented results are initial results from the first MAST-U experimental campaign. As a result, there are a few aspects which may need further investigations and optimisation in the future. For instance, operating the Super-X divertor in attached or moderately detached conditions (phase I & II) necessitated decreasing the core density significantly, which lead to the onset of various MHD modes, resulting in a split divertor leg and strike point as has been observed using the multi-wavelength imaging system, as well as infrared thermography and Langmuir probe measurements. As the DMS chordally integrates the data, it integrates the emission over the split strike leg. Initial results from the MWI suggest that the Balmer line emission from both strike legs may have slightly different dynamics, which needs further investigation using imaging. Although the strike leg splitting is not in agreement with the dual-slab emission model employed in BaSMPI [16, 15], which assumes the plasma profiles along the lines of sight are flat slabs with a certain length and a different electron temperature for the EIE and PMI emission regions than the EIR emission region. Nevertheless, BaSPMI has been shown to be robust against line-integration effects [15]. This implies that BaSPMI should still provide correct estimates (within uncertainties) of the chordally integrated parameters. Due to the low density operation, the fuelling valves had to be operated close to their cut-off point, potentially resulting in non-linear behaviour and resulting in large uncertainties in the valve calibration coefficients. This would complicate comparing discharges that are fuelled through different valves, at this time.

That said, however, the observed behaviour is general for all monitored MAST-U Super-X conditions, which have been employed at a range of plasma currents, poloidal flux expansion, toroidal flux expansion (e.g. position along tile 5) and fuelling locations. Therefore, despite the various caveats, we believe that these detachment phases and the processes involved during them are general for MAST-U Super-X operation.

5. Conclusions

This paper presents the first spectroscopic qualitative analysis results from the MAST Upgrade Super-X divertor. Our results show that detachment of the MAST-U Super-X divertor involves four distinct phases. First, the ionisation front detaches off the target, leading to the formation of a region where the molecular density increases and the molecules get vibrationally excited. That results in the formation of molecular ions (D_2^+ and/or $D_2^- \rightarrow D^- + D$) and those ions subsequently react with the plasma, resulting excited atoms that emit atomic hydrogen line emission as well as Molecular Activated Recombination (MAR) and Dissociation (MAD). Secondly, the peak in hydrogen line emission from those plasma-molecule interactions detaches from the target, leaving a region where the plasma is too cold to provide significant vibrational excitation (e.g. a sub-eV plasma). Thirdly, strong contributions of electron-ion recombination to the hydrogen line emission start to develop. Fourthly, the emission contributions from electron-ion recombination start to detach from the target, suggesting the movement of an electron density front. These observations have been motivated through quantitative analysis as well as by simulating the expected Balmer line emission behaviour using a simplified emission model combined with scalings of various particle densities with T_e using SOLPS-ITER simulations from both MAST Upgrade as well as the TCV tokamak.

Evidence is presented during phases 3 and 4 of strongly sub-eV temperatures, with some evidence suggesting electron temperatures between 0.1 and 0.2 eV. The electron density is modest throughout phases 1-3 ($n_e < 2 \times 10^{19} m^{-3}$), reaching levels of $n_e \ll 1 \times 10^{19} m^3$ in phase IV below the density front.

We have investigated the utility of using D_2 Fulcher emission brightnesses to obtain more information about the plasma and have shown that it can be used as a temperature indicator and it may be used as a proxy for the ionisation region. That information, combined with spectroscopic analysis, facilitated separating out the electron-impact excitation emission from emission arising from excited hydrogen atoms after molecular break-up involving molecular ions. As the contribution of plasma-molecule interactions to the hydrogen Balmer line emission is particularly strong for MAST-U, accounting for this in the interpretation of hydrogen emission diagnostics is critical.

6. Acknowledgements

This work has been carried out within the framework of the EUROfusion Consortium, funded by the European Union via the Euratom Research and Training Programme (Grant Agreement No 101052200 — EUROfusion), from the RCUK Energy Programme and EPSRC Grants EP/T012250/1 and EP/N023846/1. It has been supported in part by the Swiss National Science Foundation. To obtain further information on the data and models underlying this paper please contact publicationsmanager@ukaea.uk. Views and opinions expressed are however those of the author(s) only and do not necessarily reflect those of the European Union or the European Commission. Neither the European Union nor the European Commission can be held responsible for them.

7. References

[1] Loarte A, Lipschultz B, Kukushkin A, Matthews G, Stangeby P, Asakura N, Counsell G, Federici G, Kallenbach A, Krieger K *et al.* 2007 *Nuclear Fusion* **47** S203–S263

[2] Wenninger R, Bernert M, Eich T, Fable E, Federici G, Kallenbach A, Loarte A, Lowry C, McDonald D, Neu R *et al.* 2014 *Nuclear Fusion* **54** 114003

[3] Verhaegh K, Lipschultz B, Harrison J, Duval B, Fil A, Wensing M, Bowman C, Gahle D, Kukushkin A, Moulton D, Perek A, Pshenov A, Federici F, Février O, Myatra O, Smolders A, Theiler C, the TCV Team and the EUROfusion MST1 Team 2021 *Nuclear Fusion* **61** 106014 URL `https://doi.org/10.1088/1741-4326/ac1dc5`

[4] Lipschultz B, L Para F and Hutchinson I 2016 *Nuclear Fusion* **56** 056007 ISSN 0029-5515 URL `http://stacks.iop.org/0029-5515/56/i=5/a=056007`

[5] Moulton D, Harrison J, Lipschultz B and Coster D 2017 *Plasma Physics and Controlled Fusion* **59** 065011 ISSN 0741-3335

[6] Havlickova E, Harrison J, Lipschultz B, Fishpool G, Kirk A, Thornton A, Wischmeier M, Elmore S and Allan S 2015 *Plasma Physics and Controlled Fusion* **57** 115001 ISSN 0741-3335 URL `<Go to ISI>://WOS:000374538100002` `http://iopscience.iop.org/article/10.1088/0741-3335/57/11/115001/pdf`

[7] Theiler C, Lipschultz B, Harrison J, Labit B, Reimerdes H, Tsui C, Vijvers W A J, Boedo J A, Duval B P, Elmore S, Innocente P, Kruezi U, Lunt T, Maurizio R, Nespoli F, Sheikh U, Thornton A J, van Limpt S H M, Verhaegh K, Vianello N, Team T and Team E M

2017 *Nuclear Fusion* **57** 072008 ISSN 0029-5515 URL `<Go to ISI>://WOS:000398746200001` `http://iopscience.iop.org/article/10.1088/1741-4326/aa5fb7/pdf`

[8] Valanju P M, Kotschenreuther M, Mahajan S M and Canik J 2009 *Physics of Plasmas (1994-present)* **16** 056110

[9] Militello F, Aho-Mantila L, Ambrosino R, Body T, Bufferand H, Calabro G, Ciraolo G, Coster D, Di Gironimo G, Fanelli P *et al.* 2021 *Nuclear Materials and Energy* **26** 100908 ISSN 2352-1791

[10] Morris W, Harrison J, Kirk A, Lipschultz B, Militello F, Moulton D and Walkden N 2018 *IEEE Transactions on Plasma Science* **46** 1217–1226

[11] Fishpool G, Canik J, Cunningham G, Harrison J, Katramados I, Kirk A, Kovari M, Meyer H and Scannell R 2013 *Journal of Nuclear Materials* **438** S356–S359 ISSN 0022-3115 proceedings of the 20th International Conference on Plasma-Surface Interactions in Controlled Fusion Devices URL `https://www.sciencedirect.com/science/article/pii/S0022311513000755`

[12] Harrison J, Akers R, Allan S, Allcock J, Allen J, Appel L, Barnes M, Ayed N B, Boeglin W, Bowman C *et al.* 2019 *Nuclear Fusion* **59** 112011

[13] Fil A, Lipschultz B, Moulton D, Dudson B D, Février O, Myatra O, Theiler C, Verhaegh K, Wensing M and and 2020 *Plasma Physics and Controlled Fusion* **62** 035008

[14] Verhaegh K, Lipschultz B, Harrison J R, Duval B P, Bowman C, Fil A, Gahle D S, Moulton D, Myatra O, Perek A, Theiler C and Wensing M 2021 *Nuclear Materials and Energy* **26** 100922

[15] Verhaegh K, Lipschultz B, Bowman C, Duval B P, Fantz U, Fil A, Harrison J R, Moulton D, Myatra O, Wünderlich D, Federici F, Gahle D S, Perek A, Wensing M and and 2021 *Plasma Physics and Controlled Fusion* **63** 035018

[16] Verhaegh K, Lipschultz B, Duval B, Fil A, Wensing M, Bowman C and Gahle D 2019 *Plasma Phys. Control. Fusion* **61**

[17] Feng X, Calcines A, Sharples R M, Lipschultz B, Perek A, Vijvers W A J, Harrison J R, Allcock J S, Andrebe Y, Duval B P and Mumgaard R T 2021 *Review of Scientific Instruments* **92** 063510 (*Preprint* `https://doi.org/10.1063/5.0043533`) URL `https://doi.org/10.1063/5.0043533`

[18] Perek A, Vijvers W A J, Andrebe Y, Classen I G J, Duval B P, Galperti C, Harrison J R, Linehan B L, Ravensbergen T, Verhaegh K and de Baar M R 2019 *Review of Scientific Instruments* **90** 123514

[19] Verhaegh K, Lipschultz B, Duval B P, Harrison R, Reimerdes H, Theiler C, Labit B, Maurizio R, Marini C, Nespoli F, Sheikh U, Tsui C K, Vianello N, Vijvers W A J and Team T T E M 2017 *Nuclear Materials and Energy* **12** 1112–1117 ISSN 2352-1791

[20] Verhaegh K, Lipschultz B, Duval B, Février O, Fil A, Theiler C, Wensing M, Bowman C, Gahle D, Harrison J *et al.* 2019 *Nuclear Fusion* **59**

[21] Janev R K and Reiter D 2018 Isotope effects in molecule assisted recombination and dissociation in divertor plasmas Jülich report - juel 4411 Forschungszentrum Jülich GmbH Jülich englisch URL `https://juser.fz-juelich.de/record/850290/files/J%C3%BCl_4411_Reiter.pdf?version=1`

[22] Reiter D 2000 The data file AMJUEL: Additional atomic and molecular data for EIRENE Tech. rep. Forschungszentrum Jülich GmbH URL `http://www.eirene.de/html/amjuel.html`

[23] Lomanowski B A, Meigs A G, Sharples R M, Stamp M, Guillemaut C and Contributors J 2015 *Nuclear Fusion* **55** 123028 ISSN 0029-5515 URL `<Go to ISI>://WOS:000366534500030` `http://iopscience.iop.org/article/10.1088/0029-5515/55/12/123028/pdf`

[24] Lipschultz B, Terry J L, Boswell C, Hubbard A, LaBombard B and Pappas D A 1998 *Physical Review Letters* **81** 1007–1010 ISSN 0031-9007 URL `<Go to ISI>://WOS:000075130400019` `https://journals.aps.org/prl/abstract/10.1103/PhysRevLett.81.1007`

[25] Terry J L, Lipschultz B, Pigarov A Y, Krasheninnikov S I, LaBombard B, Lumma D, Ohkawa H, Pappas D and Umansky M 1998 *Physics of Plasmas* **5** 1759–1766 ISSN 1070-664x

[26] Kunze H J 2009 *Introduction to plasma spectroscopy* vol 56 (Springer)

[27] Clark J G, Bowden M D and Scannell R 2021 *Review of Scientific Instruments* **92** 043545 (*Preprint* `https://doi.org/10.1063/5.0043813`) URL `https://doi.org/10.1063/5.0043813`

[28] O'Mullane M 2013 Adas: Generalised collisonal radiative data for hydrogen Tech. rep. ADAS URL `http://www.adas.ac.uk`

[29] Myatra O, Moulton D, Fil A, Dudson B and Lipschultz B 2018 Taming the flame: Detachment access and control in mast-u super-x *Plasma Surface Interactions* URL `https://fusion-cdt.ac.uk/wp-content/uploads/2018/08/Myatra-Omkar-psi_poster.pdf`

[30] Fil A M D, Dudson B D, Lipschultz B, Moulton D, Verhaegh K H A, Fevrier O and Wensing M 2017 *Contributions to plasma physics* **58** ISSN 0863-1042

[31] Perek A, Linehan B, Wensing M, Verhaegh K, Classen I, Duval B, Février O, Reimerdes H, Theiler C, Wijkamp T and de Baar M 2021 *Nuclear Materials and Energy* **26** 100858 ISSN 2352-1791

[32] Reimerdes H, Duval B, Elaian H, Fasoli A, Février O, Theiler C, Bagnato F, Baquero-Ruiz M, Blanchard P, Brida D *et al.* 2021 *Nuclear Fusion* **61** 024002

[33] Ravensbergen T, van Berkel M, Silburn S A, Harrison J R, Perek A, Verhaegh K, Vijvers W A J, Theiler C, Kirk A and de Baar M 2020 *Nuclear Fusion* URL `https://doi.org/10.1088%2F1741-4326%2Fab8183`

[34] Ravensbergen T, van Berkel M, Perek A, Galperti C, Duval B, Février O, van Kampen R, Felici F, Lammers J, Theiler C *et al.* 2021 *Nature communications* **12** 1–9

[35] Reiter D, Baelmans M and Börner P 2005 *Fusion Science and Technology* **47** 172–186 ISSN 1536-1055

[36] Holm A, Wünderlich D, Groth M and Börner P *Contributions to Plasma Physics* **n/a** e202100189 (*Preprint* `https://onlinelibrary.wiley.com/doi/pdf/10.1002/ctpp.202100189`) URL `https://onlinelibrary.wiley.com/doi/abs/10.1002/ctpp.202100189`

[37] Summers H P, Dickson W J, O'Mullane M G, Badnell N R, Whiteford A D, Brooks D H, Lang J, Loch S D and Griffin D C 2006 *Plasma Physics and Controlled Fusion* **48** 263–293 ISSN 0741-3335 1361-6587

[38] Lomanowski B, Groth M, Coffey I H, Karhunen J, Maggi C F, Meigs A, Menmuir S and O'Mullane M 2020 *Plasma Physics and Controlled Fusion* **62**

[39] Lomanowski B, Carr M, Field A, Groth M, Henderson S, Harrison J, Huber A, Jarvinen A, Lawson K, Lowry C *et al.* 2019 *Nuclear Materials and Energy* **20**

[40] Soukhanovskii V, Khrabry A, Scott H, Moulton D and Harrison J 2019 *Bulletin of the American Physical Society* **64**

[41] Stangeby P C and Chaofeng S 2017 *Nuclear Fusion* **57** 056007 ISSN 0029-5515

[42] Wünderlich D, Scarlett L H, Briefi S, Fantz U, Zammit M C, Fursa D V and Bray I 2021 *Journal of Physics D: Applied Physics* **54** 115201 URL `https://doi.org/10.1088/1361-6463/abccf2`

[43] Wünderlich D, Giacomin M, Ritz R and Fantz U 2020 *Journal of Quantitative Spectroscopy and Radiative Transfer* **240** 106695 ISSN 0022-4073

[44] Wünderlich D and Fantz U 2016 *Atoms* **4** ISSN 2218-2004

[45] Laporta V, Agnello R, Fubiani G, Furno I, Hill C, Reiter D and Taccogna F 2021 *Plasma Physics and Controlled Fusion*

[46] Wensing M, Duval B, Fevrier O, Fil A, Galassi D, Havlickova E, Perek A, Reimerdes H, Theiler C, Verhaegh K and Wischmeier M 2019 *Plasma Phys. Control. Fusion* **61**

Appendix A. Simplified emission modelling

The simplified emission trends shown in figure 9 have been modelled using scalings obtained from SOLPS-ITER simulations for the behaviour of the molecular density, neutral atom density and the respective pathlengths as function of T_e. Using those scalings with a plasma slab model (such as employed by BaSPMI [15, 16, 19]), the hydrogen line brightnesses for electron-impact excitation (EIE), electron-ion recombination (EIR) and plasma-molecule interactions (PMI) can be calculated as indicated in equation A.1, where

$f_{\Delta L n_D/n_e}$, $f_{\Delta L_{rec}}$ and $f_{\Delta L n_{D_2}/n_e}$ are the scalings used. Those scalings are analogously derived as in [16].

$$\begin{aligned} B^{EIE}_{n\to 2} &= n_e^2(\Delta L n_H/n_e)PEC^{EIE}_{n\to 2}(n_e,T_e) = n_e^2 f_{\Delta L n_D/n_e}(T_e)PEC^{EIE}_{n\to 2}(n_e,T_e) \\ B^{EIR}_{n\to 2} &= n_e^2(\Delta L)PEC^{EIR}_{n\to 2}(n_e,T_e) = n_e^2 f_{\Delta L_{rec}}(T_e)PEC^{EIR}_{n\to 2}(n_e,T_e) \\ B^{PMI}_{n\to 2} &= n_e^2(\Delta L n_{D_2}/n_e)PEC^{PMI}_{n\to 2}(n_e,T_e) = n_e^2 f_{\Delta L n_{D_2}/n_e}(T_e)PEC^{PMI}_{n\to 2}(n_e,T_e) \end{aligned} \tag{A.1}$$

$f_{\Delta L n_H/n_e}$, $f_{\Delta L_{rec}}$ and $f_{\Delta L n_{D_2}/n_e}$ have been obtained using synthetic diagnostic techniques employed to both TCV as well as MAST-U SOLPS-ITER simulations, which provide us with a synthetic brightness "measurement" of $B^{EIE}_{n\to 2}$, $B^{EIR}_{n\to 2}$ and $B^{PMI}_{n\to 2}$. Using the $D\alpha$ *emissivity* weighted n_e and T_e along each line of sight, $f_{\Delta L n_D/n_e}$, $f_{\Delta L_{rec}}$ and $f_{\Delta L n_{D_2}/n_e}$ can be calculated for every diagnostic chord and every SOLPS-ITER simulation. For MAST-U both the V1 and V2 views have been used to compute these relations (figure 2). Using the obtained database for those parameters for TCV (density scan) and MAST-U (density scan and N_2 seeding), a linear fit in logarithmic space [41, 15] is performed through the obtained database for $f_{\Delta L n_H/n_e}$, $f_{\Delta L_{rec}}$ and $f_{\Delta L n_{D_2}/n_e}$ to obtain the used scalings, shown in equation A.2 and figure A1 as function of temperature.

$$\begin{aligned} f^{MAST-U}_{\Delta L n_D/n_e}(T_e) &= 10^{-1.4721-1.126\log 10(T_e)} \text{ m} \\ f^{TCV}_{\Delta L n_D/n_e}(T_e) &= 10^{-2.7442-0.658\log 10(T_e)} \text{ m} \\ f^{MAST-U}_{\Delta L n_{D_2}/n_e}(T_e) &= 10^{-1.176-2.3075\log 10(T_e)} \text{ m} \\ f^{TCV}_{\Delta L n_{D_2}/n_e}(T_e) &= 10^{-2.7907-1.6965\log 10(T_e)} \text{ m} \\ f^{MAST-U}_{\Delta L_{rec}} &= 10^{-0.2609} \text{ m} \\ f^{TCV}_{\Delta L_{rec}} &= 10^{-1.0224} \text{ m} \end{aligned} \tag{A.2}$$

The emission coefficients were obtained using ADAS [28, 37] ($PEC^{PMI}_{n\to 2}$ & $PEC^{PMI}_{n\to 2}$) and Yacora (on the Web) [42, 43, 44] ($PEC^{PMI}_{n\to 2}$). $PEC^{PMI}_{n\to 2}$ is an effective emission coefficient which accounts for interactions involving D_2, D_2^+ and D^-: $PEC^{PMI}_{n\to 2}(n_e,T_e) = PEC^{D_2}_{n\to 2}(n_e,T_e) + \frac{n_{D_2^+}}{n_{D_2}}PEC^{D_2^+}_{n\to 2}(n_e,T_e) + \frac{n_D{}^-}{D_2}PEC^{D^-}_{n\to 2}(n_e,T_e)$, where $\frac{n_{D_2^+}}{n_{D_2}}$ and $\frac{n_{D-}}{n_{D_2}}$ are the ratios between the D_2^+ and D^- densities to the D_2 density, respectively. Those ratios are modelled as function of n_e and T_e using AMJUEL [22, 21, 15, 3] (H12 2.2.0c and H11 7.2.0c respectively). However, those AMJUEL rates are specifically derived for hydrogen and not deuterium. Following previous work [21], the hydrogen rates are remapped to the deuterium rates by multiplying them with 0.95 and 0.7 respectively. One caveat is that the obtained ratios are highly sensitive to the distribution of vibrational states, for which a simplified model is employed to create those AMJUEL rates. Different results may be obtained with a more realistic model [3, 45].

The Fulcher brightness (arbitrary units) is modelled using $\propto n_{D_2}PEC^{Fulcher}_{D_2}(n_e,T_e)$, where the Fulcher emission coefficient is obtained from AMJUEL [22] (H12 2.2.5fl).

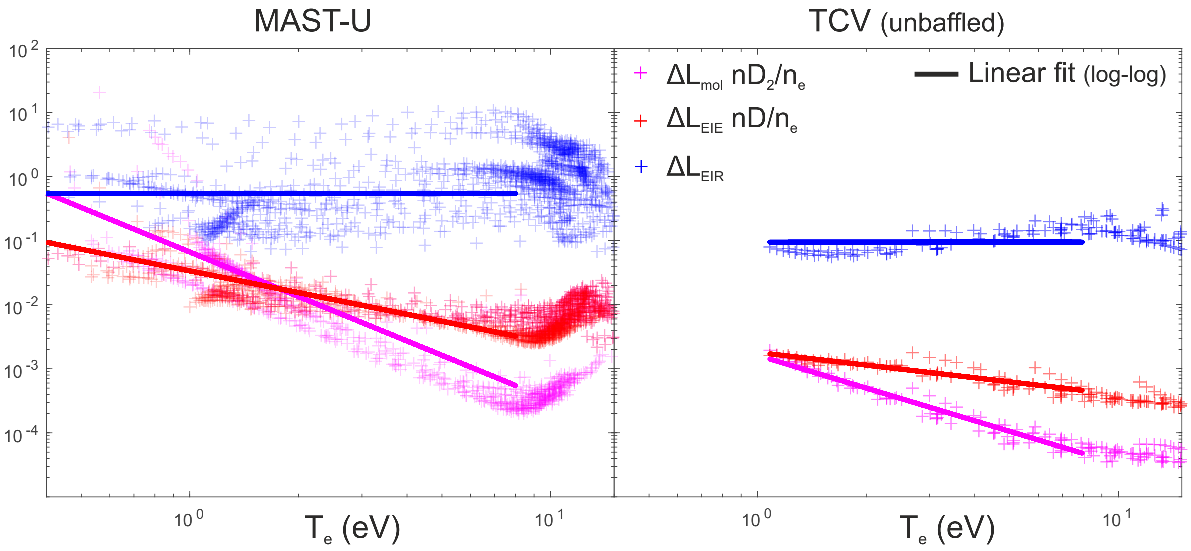

Figure A1. Scalings of $f^{MAST-U}_{\Delta L n_D/n_e}(T_e)$, $f^{TCV}_{\Delta L n_D/n_e}(T_e)$, $f^{MAST-U}_{\Delta L n_{D_2}/n_e}$, $f^{TCV}_{\Delta L n_{D_2}/n_e}$, $f^{MAST-U}_{\Delta L_{rec}}$, $f^{TCV}_{\Delta L_{rec}}$ obtained from SOLPS-ITER [30, 29] using synthetic diagnostics [16, 15, 46] as function of their respective temperatures (excitation temperature for EIE, PMI and recombination temperature for EIR).

Appendix B. Fulcher constraint calculation

The Fulcher profile as function of T_e are computed using the simplified emission modelling in Appendix A. The resultant emission profile as function of temperature will peak at a certain temperature and decay towards lower temperatures. These profiles are normalised with respect to their peak and the temperatures at the decaying (low T_e) end of the profile, corresponding to 1 % to 80 % of the peak brightness, are recorded. The reason this range is used is that close to the the peak brightness, the difference between the peak and the reference point could be too small to comfortably detect the reference point. Likewise, below a certain point, the signal to noise ratio likely prohibits comfortably detecting the correct reference point. To reduce the sensitivity of this method to a density evolution as function of T_e, we divide the Fulcher band brightness by the electron temperature ($B_{Fulcher}/n_e \propto \frac{n_e \Delta L n_{D_2} PEC_{Fulcher}(n_e,T_e)}{n_e} = \Delta L n_{D_2} PEC_{Fulcher}(n_e,T_e)$). This leads to a T_e curve as function of % of the $\frac{B_{Fulcher}}{n_e}(T_e)$ profile (at a single n_e).

Monte Carlo uncertainty propagation (similar to BaSPMI analysis [16, 15]) is applied where a $\pm(1+0.4)$ uncertainty is applied to slope of the $n_{D_2}\Delta L$ scaling (in log-log space where 0.4 is the difference in slope in log-log space between the MAST-U and TCV scalings (equation A.2)) and a density range of $10^{18} - 2 \cdot 10^{20}$ m^{-3} is assumed. A random uncertainty of 0.5 eV is applied to the recorded temperature corresponding to a certain fraction of the peak brightness (e.g. the 'T_e vs % of the $\frac{B_{Fulcher}}{n_e}(T_e)$ profile' curve - figure 10). A kernel density estimator is used to map the resultant distributions to probability density distributions, from which the most likely value as well as the lower/upper bounds spanning a 68 % confidence interval are extracted, leading to the curves shown in figure 10.

Appendix C. BaSPMI analysis set-up

BaSPMI [15] has been used in this work to separate the $D\alpha$ emission profile into its various atomic and molecular contributions (figure 4). The BaSPMI analysis is performed using the measured brightnesses shown in figure 4 ($n = 3, 5, 6$ Balmer line emission). Instead of $D\beta$ measurements (which are not available for this specific discharge), the separation between D_2^+ and D^- is modelled using AMJUEL [22] (similar to the emission model used in Appendix A).

To facilitate these preliminary BaSPMI calculations on MAST-U, various simplifying assumptions are made. First, instead of estimating ΔL based using the width of the ion saturation current profile near the target, an assumed width near the target of 10 cm is used (from the separatrix towards the low-field-side). ΔL is then computed by calculating the intersections between the line of sight and the flux surfaces corresponding to this width. The lower/upper ranges of ΔL (68 % confidence interval) are set to 33 and 133 % of ΔL, respectively, and are used in the uncertainty propagation. Secondly, given the low electron densities on MAST-U and the fact that for # 45371 a medium spectral resolution setting was used to measure the n=5,6 Balmer lines simultaneously, a large uncertainty is assigned to the Stark broadening inferred electron densities of $2 \cdot 10^{19}$ m^{-3} (68 % confidence interval). To ensure that this does not lead to erroneous high electron density, an upper electron density cap of $3 \cdot 10^{19}$ m^{-3} is introduced with a lower cut-off at $2 \cdot 10^{18}$ m^{-3}. The inferred electron densities for # 45371 are around $0.8 - 2.5 \cdot 10^{19}$ m^{-3}, which are somewhat higher than those obtained from divertor Thomson scattering ($0.5 - 1 \cdot 10^{19}$ m^{-3}).

To employ BaSPMI, the Fulcher band has been used to provide an excitation temperature constraint (section 4.2 and Appendix B). This is achieved by using the trailing end of the Fulcher brightness profile along the various spectroscopic chords, which are normalised with respect to the peak. After the peak of the Fulcher band brightness has left the spectroscopic view, the last known peak intensity is used for the normalisation. Using the probability density functions derived in section 4.2 and Appendix B, weights are computed for each solution determined by BaSPMI. Above/below the 80/1 % regions of the peak (of the trailing edge) of the Fulcher band emission region, the obtained PDFs are used to obtain a maximum/minimum temperature constraint, respectively. To obtain these constraints, the PDFs at the edge 80 / 1 % of the Fulcher profile peak are used up until the peak of the PDF - above / below the peak of the PDF, the same weight that corresponds to the peak of the PDF is used.

The part of the analysis that obtains an estimate of the recombinative temperature T_e^R had to be altered as the recombinative temperatures on MAST-U seem to be below the ADAS limit of 0.2 eV. As such, no suitable temperatures could be found to explain the measured recombinative emission brightness during conditions where strong recombinative emission occurs. As opposed to filtering out these results from the Monte Carlo sample, T_e^R has been set to 0.2 eV in this regime.

Given the high contribution of plasma-molecule interactions to the hydrogen emission lines on MAST-U, the BaSPMI analysis techniques, at times, struggled to obtain reasonable solutions. To facilitate filling in the solution space which is covered by the likely T_e range obtained by the Fulcher prior, the initial conditions of the analysis were altered. The initial condition used originally, is that plasma-molecule interactions do not contribute to the medium-n Balmer line emission and the analysis is performed until a converged result is obtained (which has a self-consistent split of both the medium-n Balmer lines and $D\alpha$ in terms of atomic and molecular contributions). Currently, the initial condition uses a different contribution of plasma-molecule interactions to the each of the two medium-n Balmer lines to increase the Balmer line ratio of the atomic contribution to the medium-n Balmer lines to levels expected of a plasma where electron-ion recombination dominates over electron-impact excitation - at the point where electron-ion recombination occurs.

Appendix C.1. Bayesian to BaSPMI comparison

To verify these modifications to the BaSPMI analysis, a stand-alone fully Bayesian analysis methodology has been used as well using the same emission model as BaSPMI and using priors for the excitation emission temperature based on the Fulcher band; n_e based on Stark broadening; ΔL based on the BaSPMI input for ΔL same constraints; a constraint that the excitation emission temperature should be larger than the recombination emission temperature [16]. Uncertainties in the emission coefficients are not employed in the Bayesian analysis, but are used in BaSPMI (10 % for atomic PECs and 20 % for molecular PECs). The measurements used in this Bayesian approach are the $n = 5$ brightness, the $n = 6/5$ Balmer line ratio and the $n = 3/5$ Balmer line ratio (using assumed non-correlated uncertainties of similar values as those used in BaSPMI). This is different from BaSPMI where correlated uncertainties for every brightness measurement are calculated from a multi-variate Gaussian distribution based on their absolute and relative uncertainty estimates. This results in a posterior distribution and rejection sampling is applied to obtain the same sets of output data similar to BaPSMI. To keep the number of free parameters at 6, the Bayesian implementation only includes contributions from D_2^+, D^-, electron-impact excitation and electron-ion recombination (e.g. not D_2) and employs AMJUEL to model the relative contributions between D_2^+ and D^-. To reduce the computational effort needed, the sample size is reduced to 100 in the Bayesian analysis, whereas this is 30000 in BaSPMI (effective sample size (Kish) of 100 and 2500-8000, respectively).

This is then analysed in the same way as BaSPMI (e.g. using a kernel density estimator to estimate the maximum likelihood and uncertainty margins) to obtain the same parameters as those shown in figure 4 A I-IV, which is shown in figure C1 B I-IV. The obtained result is qualitatively in agreement with BaSPMI. However, a less clear separation between plasma-molecule interactions and electron-impact excitation is obtained in the full Bayesian version and the analysis performs more poorly (compared to BaSPMI) in electron-ion recombination dominant conditions, where the analysis suggests

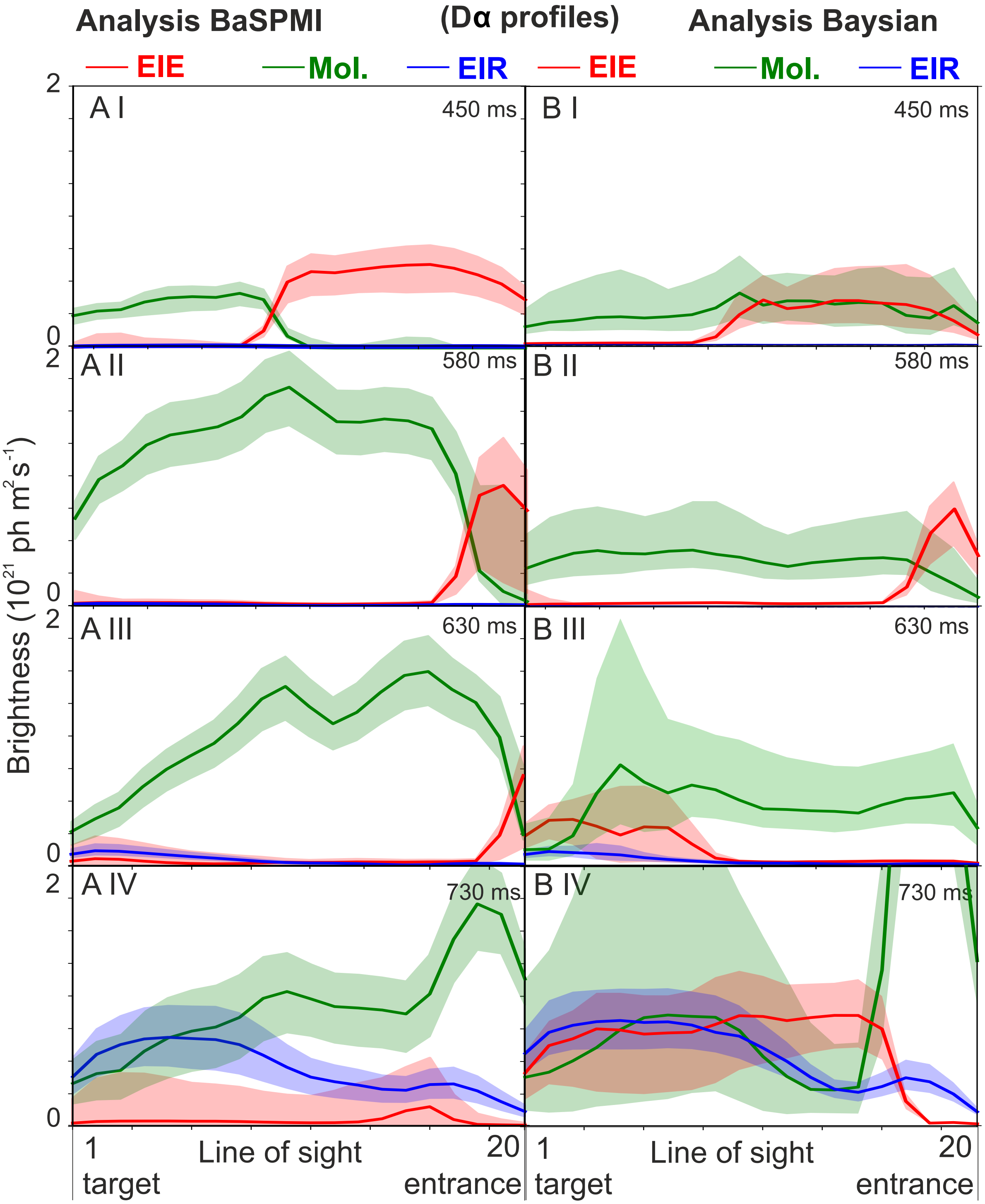

Figure C1. Comparison of figure 4 A I-IV obtained using BaSPMI and B I-IV obtained using an alternative Bayesian approach.

electron-impact excitation occurs near the target - which is nonphysical. The reason for the latter difference is that BaSPMI utilises the fact that the discharge is a fuelling scan: it assumes that F_{rec} [16] - the fraction of recombinative emission compared to the EIR + EIE Balmer line emission - cannot decrease during a discharge; which is something that cannot easily be implemented in a full Bayesian approach.

Additionally, the Bayesian analysis will struggle more with the fact that ADAS data is (currently) only available until 0.2 eV - therefore it cannot describe the EIR portion of the emission accurately ($B^{EIR,Bayesian}_{n\rightarrow 2} \approx n_e^2 \Delta LPEC^{EIR}_{n\rightarrow 2}(n_e, T_e^R)$. This is less of a problem for BaSPMI as the EIR portion of the emission is characterised using the fraction of medium-n Balmer line emission due to plasma-mol. interactions ($f^{mol}_{n\rightarrow 2}$) and the fraction of the atomic portion of the medium-n Balmer lin emission due to EIR ($F^{n\rightarrow 2}_{rec}$) - e.g. $B^{EIR,BaSPMI}_{n\rightarrow 2} = (1 - f^{mol}_{n\rightarrow 2}) \times F^{n\rightarrow 2}_{rec} B_{n\rightarrow 2}$. The Bayesian analysis compensates for this by increasing the n_e to $3 \times 10^{19} m^{-3}$ (clearly too high when compared with $< 10^{19} m^{-3}$ values from DTS as well as $< 2 \times 10^{19} m^{-3}$ values from Stark broadening) in the recombining regime while keeping T_e^R at 0.3 eV.